Interferometry based on the quantum Kibble-Zurek mechanism

Han-Chuan Kou[1,2] and Peng Li ⊙[1,2,*]

[1]*College of Physics, Sichuan University, 610064, Chengdu, People's Republic of China*
[2]*Key Laboratory of High Energy Density Physics and Technology of Ministry of Education, Sichuan University, 610064,Chengdu, People's Republic of China*

We propose an interferometry within the framework of the quantum Kibble-Zurek mechanism by exemplifying two prototypical quench protocols, namely, the round-trip and quarter-turn ones, on the transverse Ising and quantum *XY* chains. Each protocol contains two linear ramps that drive the system across quantum critical point twice. The two linear ramps arouse two respective nonadiabatic critical dynamics that are well described by the quantum Kibble-Zurek mechanism. However, in combination, the two critical dynamics can interfere with each other deeply. As an effect of the interference, the dynamical phase is exposed in the final excitation probability, which leads to a quantum coherent many-body oscillation in the density of defects with predictable characteristic period. Thus, such an interference is available for direct experimental observations. In the quantum *XY* model, we show that an interference can also arise from the interplay between two different critical dynamics derived from a critical point and a tricritical point. Furthermore, we demonstrate a phenomenon of multiple length scales in the defect-defect correlator, which is due to the interplay between the interference and the quantum dephasing of excited quasiparticle modes. It turns out that the dephased result relies on how the diagonal and off-diagonal lengths are modulated by the controllable parameters in a quench protocol.

I. INTRODUCTION

The Kibble-Zurek mechanism (KZM) was first proposed in a cosmological setting [1,2], which reflects the nonadiabatic nature of the critical dynamics in symmetry-breaking phase transitions. Later, its scenario for the creation of topological defects was disclosed to be remarkably adaptable to condensed matter systems being quenched [3–5], which paves the way to experimental tests [6–19]. As the analog in quantum phase transitions, quantum KZM (QKZM) [20–24] attracts lots of attention in recent years. Significant progresses in both theory [25–48] and experiment [49–62] have been made.

The QKZM is well demonstrated by transverse Ising chain, which can be analyzed thoroughly [23] and emulated by experiment on Rydberg atoms [59]. As an integrable model, its many-body state can be reduced to different modes (quasiparticles) so that the quench dynamics is mapped to the two-state Landau-Zener transition problem. This scenario is widely applicable to similar systems, whose quench dynamics can be mapped to multistate Landau-Zener transition problem [63,64]. Studies of quenches have been to a large extent concentrating on the density of defects that is accessible to experiments. The density of defects is counted by summing up all pairs of excited quasiparticles. In a quench protocol, most modes evolve adiabatically as a superposition of the ground and excited states, while the nearly gapless modes evolve nonadiabatically, which results in eternal defects in the final many-body state. The nonadiabatic dynamics in the transverse Ising chain is ensured by its energy gap closing near the quantum critical point (QCP) [65,66]. In practice, given that the system is linearly ramped from its initial ground state across the QCP at a slow but uniform rate controlled by the quench time τ_Q, we can parametrize this linear ramp in a smooth form $\varepsilon(t) = (t - t_c)/\tau_Q$, where $\varepsilon(t)$ is a dimensionless distance from the QCP and t_c marks the time when the QCP is crossed. Generally, QKZM states that the final density of defects scales like $n \propto \tau_Q^{-d\nu/(1+z\nu)}$, where d is the number of space dimensions, z and ν are the dynamical and the correlation length exponents, respectively [24]. This conclusion means that the quench time sets a fundamental length scale. Specifically, for the quantum Ising chain ($d = 1$) in a transverse field, the density of defects is related to the so-called KZ correlation length $\hat{\xi} \propto \sqrt{\tau_Q}$ by the relation $n \propto \hat{\xi}^{-1}$ since we have $z = 1$ and $\nu = 1$ [67–70]. It is worth noting that each pair of excited quasiparticles acquires a dynamical phase, which contains a second scale of length, $\sqrt{\tau_Q \ln \tau_Q}$. To fully characterize the quantum state after quench, we must involve both of the two scales of length [48,71].

On the other hand, a kind of quantum interference in the defect dynamics was brought up by designed quench protocol [31] and subsequent investigations demonstrated that the dynamical phase can play a vital role in the interference [36,72]. Soon afterwards, the phenomenon of dynamical freezing due to the interference was proposed in noninteracting spin systems [73] and verified by experiment later [74]. It was also shown that a periodically driven system by

*lipeng@scu.edu.cn

interference asymptotically approaches a time-periodic steady state at long times [75] and quantum interference is applicable to periodic Gibbs' ensembles in Ising-type free-fermionic systems [76]. In interacting systems, stabilization of Floquet phases by repeated interference was demonstrated [77–80]. In the last decade or so, quantum interference has extended to the entire field of the statistical mechanics of stable Floquet quantum matter [78,81]. Recently, a relevant work showed that the dynamical phase influences the coherent many-body oscillations of transverse magnetization due to interference [82].

In this work, we propose a concise interference effect induced by two successive critical dynamics. We demonstrate this effect by applying appropriate quench protocols to the transverse Ising and quantum XY chains. Each protocol consists of two linear ramps that conform to the QKZM [23,39,62]. The interference leads to an exposure of the dynamical phase in the final excitation probability, so that an oscillatory behavior in the density of defects can be observed directly. More intriguingly, we shall further disclose a remarkable phenomenon of multiple length scales in the defect-defect correlator, which reflect the intricate quantum dephasing of the excited quasiparticle modes in the final state.

The remainder of this paper is organized as follows. Two prototypical quench protocols, the round-trip and quarter-turn ones, are presented in Secs. II and III, respectively. We demonstrate in detail the effect and mechanism of interference by the former and show a flexible way to realize the interference by the latter. In Sec. IV, we reveal an associate phenomenon of multiple length scales in the defect-defect correlator. At last, a brief summary and discussion is given in Sec. V.

II. TRANSVERSE ISING CHAIN

In this section, a *round-trip quench protocol* is designed for the transverse Ising chain, which displays the essential elements for realizing the interference effect within the framework of QKZM. We present the details of solution for the quench protocol and elucidate the interference effect through the analysis of the final excitation probability and density of defects. The occurrence of interference is attributed to the mechanism of two successive Landau-Zener transitions. A *reversed round-trip quench protocol* is also discussed at last.

A. The model and round-trip quench protocol

The transverse field quantum Ising chain reads as

$$H = -\sum_{j=1}^{N} \left(J\sigma_j^x \sigma_{j+1}^x + g\sigma_j^z \right), \quad (1)$$

where σ_j^a ($a = x, y, z$) are Pauli matrices and the total number of lattice sites N is assumed to be even. The periodic boundary condition $\sigma_{N+j}^a = \sigma_j^a$ is imposed here. We only consider the ferromagnetic case (i.e., $J > 0$) and will henceforth set the reference energy scale as $J = 1$. By the Jordan-Wigner transformation,

$$\sigma_j^z = 1 - 2c_j^+ c_j, \quad \sigma_j^x = -(c_j^+ + c_j) \prod_{l<j} \sigma_l^z, \quad (2)$$

where the spinless fermionic operators satisfy the anticommutation relations $\{c_j, c_l^\dagger\} = \delta_{jl}$ and $\{c_j^\dagger, c_l^\dagger\} = \{c_j, c_l\} = 0$, we can transform the Hamiltonian in Eq. (1) to

$$H = P^+ H^+ + P^- H^-, \quad (3)$$

where $P^\pm = \frac{1}{2}(1 \pm \prod_{j=1}^{N} \sigma_j^z)$ are projectors on the subspaces with even ($+$) and odd ($-$) parities and the corresponding fermionic Hamiltonians read as

$$H^\pm = \sum_{j=1}^{N} \left(c_j c_{j+1} - c_j^\dagger c_{j+1} + g c_j^\dagger c_j - \frac{g}{2} + \text{H.c.} \right). \quad (4)$$

In H^-, the periodic boundary conditions $c_{N+1} = c_1$, and in H^+, the antiperiodic boundary conditions $c_{N+1} = -c_1$, must be obeyed respectively. It is noteworthy that the ground state exhibits even parity for any nonzero value of g and the parity is a good quantum number.

Because the quench process that we will concentrate on begins in the ground state, we can confine our discussion to H^+. Adopting the same convention as the one in Ref. [65],

$$c_j = \frac{1}{\sqrt{N}} e^{-i\pi/4} \sum_q e^{iqj} c_q, \quad (5)$$

$$q = -\pi + \frac{(2j-1)\pi}{N}, \quad j \in \{1, \dots, N\} \quad (6)$$

we can rewrite the Hamiltonian as

$$H^+ = \sum_q \left\{ \left(c_q^\dagger, c_{-q} \right) \begin{pmatrix} \epsilon_q & \Delta_q \\ \Delta_q & -\epsilon_q \end{pmatrix} \begin{pmatrix} c_q \\ c_{-q}^\dagger \end{pmatrix} + g \right\}, \quad (7)$$

where

$$\epsilon_q = 2(g - \cos q), \quad \Delta_q = 2\sin q. \quad (8)$$

Next, by the canonical Bogoliubov transformation,

$$c_q = u_q \eta_q - v_q \eta_{-q}^\dagger, \quad (9)$$

with the coefficients satisfying

$$u_q^2 = \frac{\omega_q + \epsilon_q}{2\omega_q}, \quad v_q^2 = \frac{\omega_q - \epsilon_q}{2\omega_q}, \quad 2u_q v_q = \frac{\Delta_q}{2\omega_q}, \quad (10)$$

we can arrive at the diagonalized form of the Hamiltonian

$$H^+ = \sum_q \omega_q \left(\eta_q^\dagger \eta_q - \frac{1}{2} \right), \quad (11)$$

where the quasiparticle dispersion reads as

$$\omega_q = \sqrt{\epsilon_q^2 + \Delta_q^2}. \quad (12)$$

In the thermodynamic limit $N \to \infty$ and at zero temperature, there is a second-order quantum phase transition from a ferromagnetic state ($0 < g < 1$) with $\mathbb{Z}_2$ symmetry breaking to a quantum paramagnetic state ($g > 1$) [66]. The QCP occurs at $g_c = 1$, where the quasiparticle dispersion becomes a linear one, $\omega_q \sim 2|q - q_c|$ with critical quasimomentum $q_c = 0$, that is responsible for the dynamical exponent $z = 1$. And as depicted in Fig. 1, the energy gap between the ground state and the first excited state behaves as $\omega_0 \propto |g - g_c|$, which implies the correlation length exponent $\nu = 1$.

Suppose the system is initially prepared in the paramagnetic ground state with all spins polarized up along the
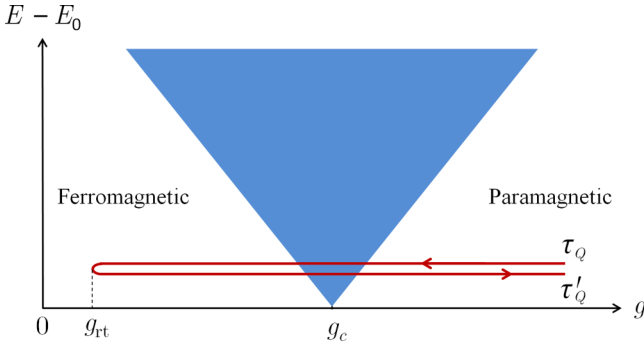
FIG. 1. Phase diagram of the transverse Ising chain and schematics of the round-trip quench protocol defined in Eq. (13). The shaded area contains all excited energy states. There is an energy gap above the ground state except at the gapless quantum critical point g_c. The round-trip quench protocol consists of two successive linear ramps. τ_Q and τ'_Q denote the quench times of the two linear ramps, respectively.

transverse field $|\uparrow, \uparrow, \ldots, \uparrow, \uparrow\rangle$, at a large enough value of $g_i \gg 1$. Then a round-trip quench protocol is applied to the system: The system is driven from the paramagnetic to the ferromagnetic regimes and returns to the paramagnetic regime in the end. This protocol contains two linear ramps: one from $g_i \equiv g(-\infty) \gg 1$ to g_{rt} ($0 \leqslant g_{rt} < 1$) in the first stage and another from g_{rt} to $g_f \gg 1$ in the second stage. As illustrated in Fig. 1, the full procedure of the round-trip quench can be parametrized as [83]

$$g \rightarrow g(t) = \begin{cases} g_{rt} - \dfrac{t}{\tau_Q} & (-\infty < t \leqslant 0), \\ g_{rt} + \dfrac{t}{\tau'_Q} & (0 < t \leqslant t_f), \end{cases} \quad (13)$$

where g_{rt} is a turning point, τ_Q and τ'_Q are quench times of the two individual linear ramps, respectively, and $t_f = (g_f - g_{rt})\tau'_Q$ is a reasonably large enough time. In the round-trip quench, the system comes across the QCP twice at $t = -(g_c - g_{rt})\tau_Q$ and $t = (g_c - g_{rt})\tau'_Q$ successively. It will be very useful to introduce the ratio

$$R = \frac{\tau'_Q}{\tau_Q}. \quad (14)$$

Throughout this paper, both τ_Q and τ'_Q are considered to be large enough and the ratio takes moderate values so that QKZM works well in each individual linear quench.

As time evolves, the system gets excited from the instantaneous ground state. We adopt the Heisenberg picture here, so the Bogoliubov quasiparticle operators do not change with time, i.e., $i\frac{d}{dt}\eta_q = 0$. The Jordan-Wigner fermions still evolve according to the Heisenberg equation $i\frac{d}{dt}c_q = [c_q, H^+]$. By a time-dependent Bogoliubov transformation,

$$c_q = u_q(t)\eta_q + v^*_{-q}(t)\eta^\dagger_{-q}, \quad (15)$$

we can arrive at the dynamical version of the time-dependent Bogoliubov–de Gennes (TDBdG) equations

$$i\frac{d}{dt}\begin{bmatrix} u_q(t) \\ v_q(t) \end{bmatrix} = \begin{bmatrix} \epsilon_q(t) & \Delta_q \\ \Delta_q & -\epsilon_q(t) \end{bmatrix}\begin{bmatrix} u_q(t) \\ v_q(t) \end{bmatrix}. \quad (16)$$

It can be solved exactly by mapping to the Laudau-Zener (LZ) problem [23]. We need to solve this problem for the round-trip quench protocol and calculate the density of defects through the excitation probability in the final state of the system. We shall adopt the long-wave approximation appropriately since only the long-wave modes within the small interval $q \lesssim \frac{1}{\sqrt{\pi \tau_Q}} \ll \frac{\pi}{2}$ can make a contribution and the short-wave modes rarely get excited during the quantum phase transition.

At last, in the paramagnetic phase with a large enough value of $g_f \gg 1$, the operator of the number of defects $\mathcal{N}_P$ measured by the deviation of spins reduces to the total number of excitations $\mathcal{N}$ approximately [39,62],

$$\mathcal{N}_P \equiv \frac{1}{2}\sum_j (1 - \sigma^z_j) \approx \mathcal{N} \equiv \sum_q \eta^\dagger_q \eta_q. \quad (17)$$

One can define the excitation probability as

$$p_q(t) = \langle \eta^\dagger_q \eta_q \rangle = |u_q(t)v_q - v_q(t)u_q|^2, \quad (18)$$

so that the density of defects is measured by

$$n = \frac{\langle \mathcal{N} \rangle}{N} = \frac{1}{N}\sum_q p_q, \quad (19)$$

where $\langle \ldots \rangle$ means the average over the final state of the system. The summation can be replaced by an integral $\frac{1}{N}\sum_q \rightarrow \int_0^\pi \frac{dq}{\pi}$. The details of solution of the TDBdG equations in Eq. (16) are put in Appendix A. We only quote the results here.

B. Interference effect at $g_{rt} = 0$

For simplicity, we dwell on the case of $g_{rt} = 0$ now, which gives a clear interference effect with many-body oscillation.

1. Final excitation probability

By Eq. (18), we work out the final excitation probability after the full round-trip quench as

$$p^f_q \equiv p_q(t_f) = A^2 + B^2 - 2AB\cos\psi, \quad (20)$$

where

$$A = e^{-\pi q^2 \tau_Q}\sqrt{1 - e^{-2\pi q^2 \tau_Q R}}, \quad (21)$$

$$B = e^{-\pi q^2 \tau_Q R}\sqrt{1 - e^{-2\pi q^2 \tau_Q}}, \quad (22)$$

$$\psi = \frac{\pi}{2} + 2(1 + R)\tau_Q + q^2\tau_Q\{(1 + R)\ln\tau_Q \\ + (1 + R)(\ln 4 + \gamma_E - 2) + R\ln R\}. \quad (23)$$

In the calculation, we have made the substitutions $\sin^2 q \approx q^2$ and $\cos^2 q \approx 1 - q^2$, according to the long-wave approximation [39]. The presence of the total dynamical phase ψ in p^f_q undoubtedly manifests an interference effect. This result is in contrast to the usual one after the first linear ramp, in which the excitation probability (at $t = 0$ here) reads as

$$p^0_q \equiv p_q(0) \approx e^{-2\pi \tau_Q q^2}, \quad (24)$$

as has been revealed by the classical works [21,23]. p^0_q reaches its peak at $q^* = \pi/N \sim 0$.
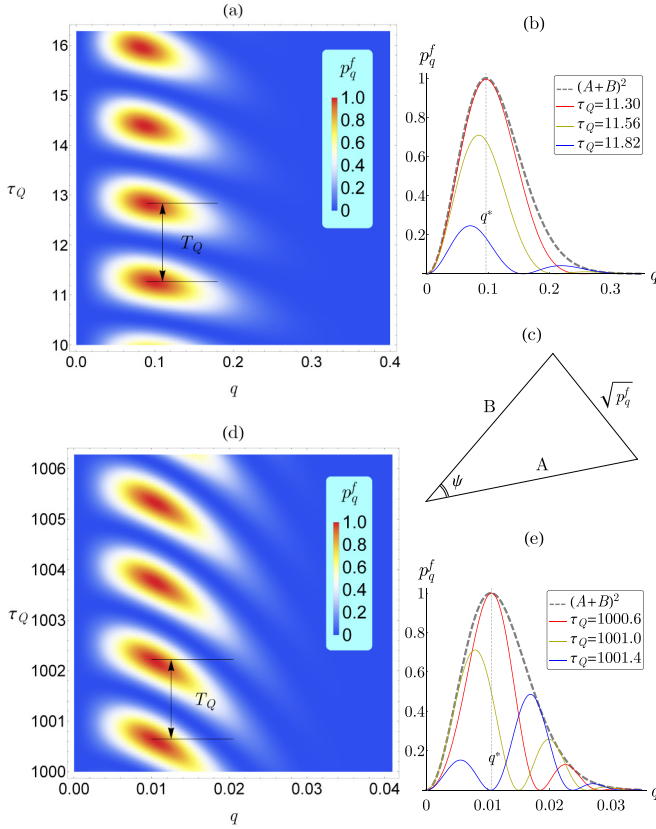
FIG. 2. Analysis of the final excitation probability p_q^f ($g_{rt} = 0$ and $R = 1$). (a), (d) Exemplify the density plots of p_q^f for $10 < \tau_Q < 16.3$ and $1000 < \tau_Q < 1006.3$, respectively, which illustrate the oscillatory behavior of p_q^f along τ_Q direction with a period $T_Q = \pi/2$ according to Eq. (27). (b), (e) Illustrate p_q^f versus q at several fixed values of τ_Q ($\tau_Q = 11.3, 11.56, 11.82$ and $\tau_Q = 1000.6, 1001, 1001.4$), where the characteristic momentum $q^* = \sqrt{\ln 2/(2\pi \tau_Q)}$ of the upper bound $(A + B)^2$ is denoted by the vertical dashed lines. (c) The graph representation of Eq. (20). Please see more details in the text.

To see through the interference taking effect after the second linear ramp, we look into the density plots of p_q^f, which shows an array of humps lining up along τ_Q direction as exemplified in Figs. 2(a) and 2(d). First of all, p_q^f takes values between lower and upper bounds,

$$(A - B)^2 \leqslant p_q^f \leqslant (A + B)^2. \tag{25}$$

For the upper bound, we can define its characteristic quasimomentum q^* by its peak position [Figs. 2(b) and 2(e)], whose value can be numerically solved from the equation

$$\frac{1 + \sqrt{2}e^{\pi(R-1)\tau_Q q^2}}{R\sqrt{R} + e^{\pi(R-1)\tau_Q q^2}} = \frac{e^{\pi(R+1)\tau_Q q^2}}{1 + R}. \tag{26}$$

For $R = 1$, the equation can be solved analytically and gives $q^* = \sqrt{\frac{\ln 2}{2\pi \tau_Q}}$. In general, we have the behavior $q^* \sim \tau_Q^{-1/2}$. When τ_Q increases, the humps become distorted with tails bending down so that more peaks along q direction can be observed for larger τ_Q as shown in Figs. 2(b) and 2(e). Second, the period of oscillation along τ_Q direction can be worked out

readily as

$$T_Q = \lim_{\tau_Q \to \infty} \frac{2\pi}{(1 + R)\{2 + (q^*)^2 \ln \tau_Q\}} = \frac{\pi}{1 + R} \tag{27}$$

because only the modes around the peaks at q^* make contributions and the value of q^* is as small as $\sim \tau_Q^{-1/2}$. In fact, this period is due to the length scale τ_Q in the total dynamical phase ψ. Another important length scale, $\tau_Q \ln \tau_Q$, in ψ affects the dephasing of the excitation modes [48], which will be discussed later. The same oscillatory behavior can also be measured by the variable τ_Q' and the corresponding period becomes

$$T_Q' = \frac{T_Q}{R} = \frac{\pi}{R(1 + R)}. \tag{28}$$

2. Oscillatory density of defects

As a more easy way to observe the effect of interference, we work out the final density of defects as

$$n = n_0 \left\{ f + \sum_{i=1}^{3} M_i \cos\left(2\pi \frac{\tau_Q}{T_Q} + \delta_i\right) \right\}, \tag{29}$$

in which

$$n_0 = \frac{1}{2\pi \sqrt{2\tau_Q}} \tag{30}$$

is a QKZM factor matching the result of usual one-way quench [23],

$$f = 1 + \frac{1}{\sqrt{R}} - \frac{2}{\sqrt{1 + R}} \tag{31}$$

is a factor without oscillation, M_i's and δ_i's are oscillation amplitudes and phases whose expressions are to be found in Appendix A. This result can be abbreviated to

$$n = n_0 \left\{ f + M \cos\left(2\pi \frac{\tau_Q}{T_Q} + \delta\right) \right\}. \tag{32}$$

To distinguish the contribution of each term, we write

$$n_0 f = \frac{1}{2\pi \sqrt{2\tau_Q}} + \frac{1}{2\pi \sqrt{2\tau_Q'}} - \frac{1}{\pi \sqrt{2(\tau_Q + \tau_Q')}}. \tag{33}$$

So it is clear to see that the former two terms in Eq. (33) are individual contributions from the two critical dynamics of linear quenches and the last term is a nonoscillatory part of interplay between the two critical dynamics. While the oscillatory part of interplay between the two critical dynamics is embedded in the cosinusoidal terms in Eq. (29) or the one in Eq. (32). The oscillatory density of defects for $R = 1$ and $2 < \tau_Q < 60$ is exemplified in Fig. 3. We see the formula in Eq. (32) obtained by long-wave approximation is in good agreement with the numerical solution of the TDBdG equations in Eq. (16). This intriguing result is in contrast to the traditional case of one-way quench [23].

In the large-τ_Q limit, the amplitude factor M becomes

$$\lim_{\tau_Q, \tau_Q' \to \infty} M = \frac{2\pi \tau_Q \sqrt{2\pi \tau_Q'}}{(\tau_Q \ln \tau_Q + \tau_Q' \ln \tau_Q')^{3/2}} \tag{34}$$
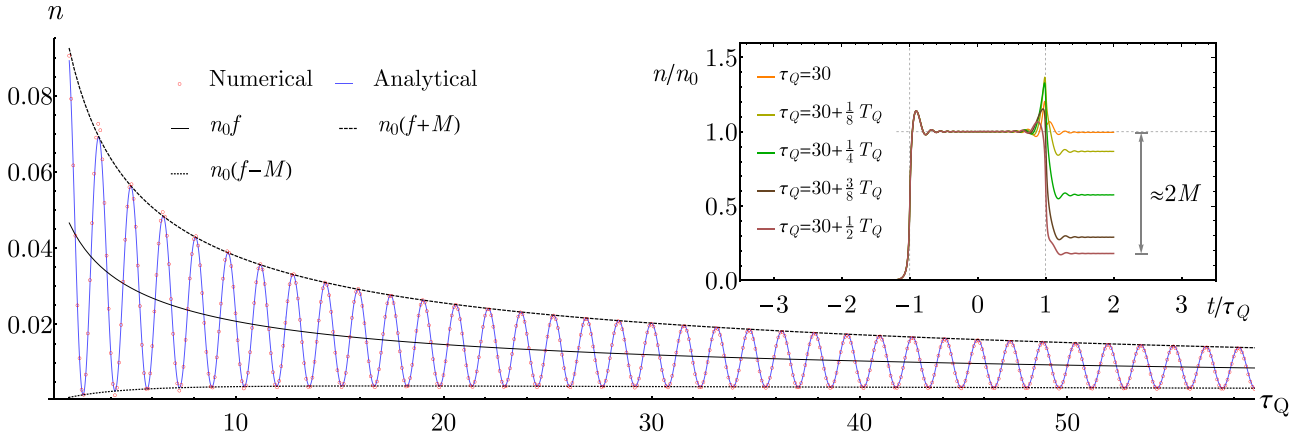
FIG. 3. Oscillatory density of defects as an effect of interference. Both analytical (blue curve) and numerical (red circles) results are illustrated for comparison, which show a good agreement. The analytical result comes from the expression in Eq. (32) and the numerical one is obtained by numerically solving the TDBdG equations in Eq. (16). The black solid line denotes the nonoscillatory part $n_0 f$ and the dashed and dotted lines denote the upper and lower bounds $n_0(f + M)$ and $n_0(f - M)$ of the density of defects. The period of oscillation is $T_Q = \frac{\pi}{2}$ according to Eq. (27) since we have $R = 1$ here. The inset shows the rescaled density of defects n/n_0 evolving with rescaled time t/τ_Q. In it, we have select several typical values of quench time within half a period, $30 \leqslant \tau_Q \leqslant 30 + \frac{T_Q}{2}$. It is clear that the density of defects is finally dispersed in a range of amplitude $n_0(f - M) \sim n_0(f + M)$.

asymptotically. To see its behavior more clear, one can get $\lim_{\tau_Q \to \infty} M \sim (\ln \tau_Q)^{-3/2}$ by setting $R = 1$. In fact, this amplitude factor is a remnant due to the interference after quantum dephasing of the excited quasiparticle modes in the final state being accomplished. To be more specific, we illustrate the density of defects evolving with time in the inset of Fig. 3, which is a numerical solution of the TDBdG equations in Eq. (16). The final state is a superposition over many quasiparticle eigenstates, whose dynamical phases rely on the quasimomentum q. The q-dependent phases become so scrambled that the dephasing is ensured providing enough time for the final state to evolve in the last adiabatic stage [48]. Meanwhile, the excitation probability p_q^f containing the total dynamical phase ψ becomes frozen after the dephasing. Henceforth, the density of defects is dispersed in a range of amplitude $n_0(f - M) \sim n_0(f + M)$.

It is noteworthy that the interplay between the interference and the dephasing also influences the correlation functions deeply and lead to a phenomenon of multiple length scales, which will be discussed later.

3. Mechanism of interference: Two successive Landau-Zener transitions

Now we look into how the quantum dynamical phase can result in an interference in the round-trip quench protocol. In fact, the interference can be attributed to a mechanism based on a theory of two successive Landau-Zener transitions. As illustrated in Fig. 4(a), the full round-trip quench process can be divided into three adiabatic and two impulse stages approximately [24]. The system is driven across QCP twice, i.e., the system undergoes nonadiabatic transitions in the two impulse regimes as represented by the shaded areas. To get a rough but clear picture, we discuss the theory in an intuitive way below.

First of all, different pairs of quasiparticles get excited independently, thus we can focus on the single-mode problem.

In the initial state, the q mode is empty and we label the state by $|0\rangle$. With time increasing, the q mode state that is labeled by $|q, -q\rangle = c_q^\dagger c_{-q}^\dagger |0\rangle$ is involved. Then we can follow the evolution of the two states only concerning the q mode. According to the standard Landau-Zener transition theory, the
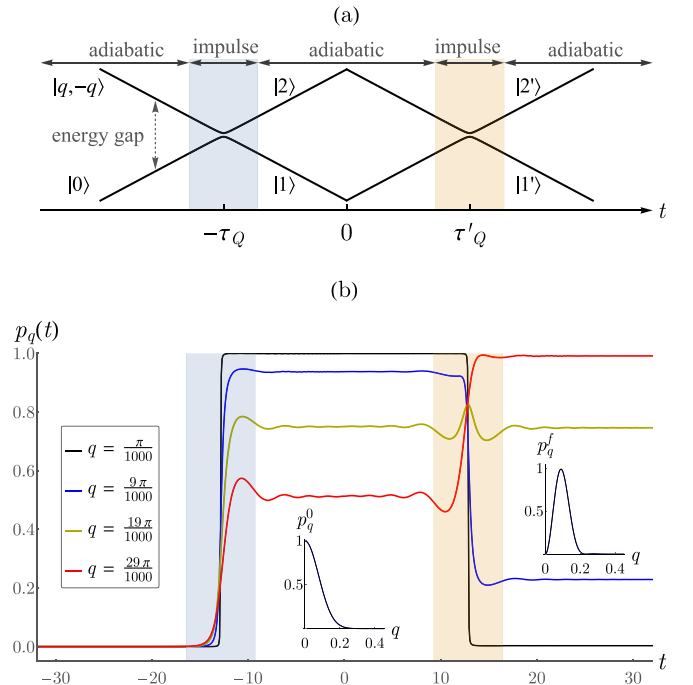

FIG. 4. (a) Two successive Landau-Zener transitions for $(q, -q)$ modes in the round-trip quench process. The full process can be roughly divided into three adiabatic and two impulse stages. (b) Evolution of the excitation probability. The final excitation probability is output for large enough time t. The two insets show a shift of peak of the excitation probability $p_q(t)$ evolving from p_q^0 to p_q^f. We have selected the parameters $R = 1$ and $\tau_Q = 12.87$ in this demonstration.

two states after the first nonadiabatic transition can be written as [84]

$$|1\rangle \sim \sqrt{1 - p_q^0}\, e^{i\theta_1}|0\rangle + \sqrt{p_q^0}\, e^{i\theta_2}|q, -q\rangle, \quad (35)$$

$$|2\rangle \sim \sqrt{p_q^0}\, e^{-i\theta_2}|0\rangle - \sqrt{1 - p_q^0}\, e^{-i\theta_1}|q, -q\rangle, \quad (36)$$

where $p_q^0 = e^{-2\pi \tau_Q q^2}$, $\theta_{1/2}$ are nonzero phases determined by the quench time τ_Q. Next, through the second nonadiabatic transition, the two states mix again and output another two new ones,

$$|1'\rangle \sim \sqrt{1 - p_q'}\, e^{i\phi_1}|1\rangle + \sqrt{p_q'}\, e^{i\phi_2}|2\rangle, \quad (37)$$

$$|2'\rangle \sim \sqrt{p_q'}\, e^{-i\phi_2}|1\rangle - \sqrt{1 - p_q'}\, e^{-i\phi_1}|2\rangle, \quad (38)$$

where $p_q' = e^{-2\pi \tau_Q' q^2}$, $\phi_{1/2}$ are other nonzero phases determined by the quench time τ_Q'.

At $t = 0$ (after the first linear quench), the excitation probability reads as

$$p_q^0 = |\langle q, -q|1\rangle|^2 = e^{-2\pi \tau_Q q^2}, \quad (39)$$

which exhibits a Gaussian peak centered at $q^* = 0$ and no information of phase remains. However, an interference is inevitable after the second nonadiabatic transition because the final excitation probability contains a nonzero phase and reads as

$$
\begin{aligned}
p_q^f &= |\langle q, -q|1'\rangle|^2 \\
&= A^2 + B^2 - 2AB \cos(\theta_1 + \theta_2 + \phi_1 - \phi_2).
\end{aligned} \quad (40)
$$

This concise result is actually the same as that in Eq. (20). It is easy to see that the phases $\theta_{1/2}$ and $\phi_{1/2}$ mimic the former ones $\theta_q^{u/v}$ and $\phi_q^{a/b}$ in Eq. (23) faithfully.

We have also calculated numerically the evolution of the excitation probability $p_q(t)$ to observe in detail how the two successive Landau-Zener transitions influence the final output. The numerical results for a system with size $N = 1000$ are illustrated in Fig. 4(b). We can observe that the mode $q = \pi/N$ approaches the saturate value 1 after the first linear ramp and drops precipitously down to 0 after the second linear ramp. And the modes $q \sim \tau_Q^{-1/2}$ indeed have the chance to be excited with a higher probability.

In short, the occurrence of interference can be attributed to the fact that the system gets excited twice in the whole quench process. But one may doubt that why there is no such a kind of interference in the quench process with the transverse field being ramped from $g = \infty$ to $-\infty$ in the transverse Ising model as depicted in previous studies [30,62,85] since the systems also get excited twice. The answer lies in that both the first and second excitations must involve the same modes to get an interference. While in the previous studies, the first and secondary excitations agitate the modes near $q_c = 0$ and π independently, thus there is no chance for such an interference to occur.

C. Interference effect at $g_{rt} = g_c = 1$

When the turning point locates at the critical point $g_{rt} = g_c = 1$, the second adiabatic stage disappears and the two

impulse stages merge. In this situation, the interference still exists, but does not induce the oscillation in the density of defects. Here, we will calculate the density of defects for $g_{rt} = 1$ and demonstrate the vanished many-body oscillation in the case based on the two-step Landau-Zener transition and the numerical result. But the analytics is a little different with $g_{rt} = 0$. We need to make use of the asymptote of $D_m(z)$,

$$\lim_{z \to 0} D_m(z) = 2^{m/2} \frac{\sqrt{\pi}}{\Gamma\left(\frac{1}{2} - \frac{m}{2}\right)}, \quad (41)$$

to get the final excitation probability containing an interference term $p_q^f \sim \cos \psi$, where the total dynamical phase turns out to be (please see details in Appendix A 3)

$$
\begin{aligned}
\psi &= \frac{\pi}{2} + \sum_a^{\frac{1}{2}, 1} \sum_T^{\tau_Q, \tau_Q'} (-1)^{2a} \arg\left\{\Gamma\left(a - \frac{i}{2}T q^2\right)\right\} \\
&\approx \frac{\pi}{2} + \frac{1}{2}\left\{\gamma_E + \gamma_d\left(\frac{1}{2}\right)\right\}(1 + R)\tau_Q q^2, \quad (42)
\end{aligned}
$$

where $\gamma_d(\frac{1}{2}) \approx -1.963\,51$ and $\gamma_d(x)$ is the digamma function. Comparing the total dynamical phase in Eq. (42) with that in Eq. (23), we find the term like $2(1 + R)\tau_Q$ does not appear in Eq. (42). Thus, the final density of defects will behave like $n \sim \tau_Q^{-1/2}$, and there is no oscillation any longer. This conclusion is similar to a previous study of the Kitaev model [36]. We have also numerically investigated the case with $g_{rt} = g_c = 1$ on a lattice as large as $N = 10\,000$ and confirmed a QKZM factor without oscillation $n \approx 0.053\tau_Q^{-0.495} \sim \tau_Q^{-1/2}$ in the final density of defects.

D. Interference effect for $0 < g_{rt} < 1$

Now we free the turning point from $g_{rt} = 0$ and 1 to the range $0 < g_{rt} < 1$ and skip the details of deduction since it is not much different from the previous one. The final excitation probability and density of defects can still be expressed by Eqs. (20) and (32). But the total dynamical phase changes to

$$
\begin{aligned}
\psi &= \frac{\pi}{2} + 2(g_{rt} - 1)^2(1 + R)\tau_Q + q^2\tau_Q(R \ln R \\
&\quad + (1 + R)[2(g_{rt} - 1) + \ln\{4\tau_Q(g_{rt} - 1)^2\} + \gamma_E]). \quad (43)
\end{aligned}
$$

As a consequence, the period of oscillation is generalized from Eq. (27) to

$$T_Q = \frac{\pi}{(g_{rt} - 1)^2(1 + R)}, \quad (44)$$

and the oscillation amplitude of the density of defects still behaves as $\lim_{\tau_Q \to \infty} M \sim (\ln \tau_Q)^{-3/2}$ asymptotically. The formula of period in Eq. (44) is numerically verified in Fig. 5 for several selected values of g_{rt}. Furthermore, we reckon that this formula also holds when $g_{rt} \to 1$ although it approaches infinity. It means that the oscillation will disappear eventually, which is consistent with the discussion on the case of $g_{rt} = 1$ in the previous subsection.

E. Reversed round-trip quench protocol

In the round-trip quench protocol elaborated above, both the starting point and ending point are located in the
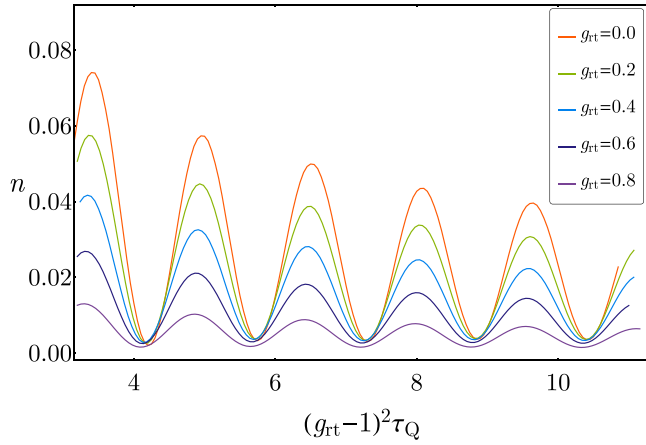
FIG. 5. Density of defects versus rescaled quench time $(g_{rt} - 1)^2 \tau_Q$. We get the results by numerically solving the TDBdG equations in Eq. (16) with parameters $R = 1$ and $g_{rt} = 0.0, 0.2, 0.4, 0.6, 0.8$. The repeated peaks and troughs justify the formula of period in Eq. (44).

paramagnetic phase. We can also consider a reversed round-trip quench protocol, which is shown in the inset of Fig. 6, for the same Hamiltonian in Eq. (1). The reversed protocol is parametrized as

$$g \to \bar{g}(t) = \begin{cases} g_{rt} + \dfrac{t}{\tau_Q} & (-g_{rt}\tau_Q < t \leqslant 0), \\ g_{rt} - \dfrac{t}{\tau'_Q} & (0 < t \leqslant g_{rt}\tau'_Q), \end{cases} \quad (45)$$

where g_{rt} is the turning point. The initial time is set at $t = -g_{rt}\tau_Q$, where the system is a classical Ising model with zero transverse field. In the first stage, the dynamics is ramped up from the ferromagnetic phase to the paramagnetic one. At $t = 0$, the transverse field reaches the turning point $g(0) = g_{rt} > 1$, where the first nonadiabatic process has been sufficiently accomplished, i.e., we would get a usual result falling in the QKZM. Then, in the second stage, the transverse field
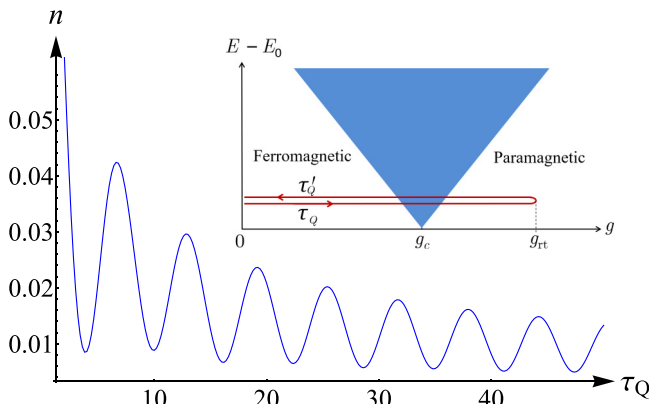

FIG. 6. Density of defects after the reversed round-trip quench protocol is applied to the transverse Ising chain with parameters $R = 1$ and $g_{rt} = 1.5$. The period of oscillation is $T_Q = 2\pi$. The inset shows the phase diagram of the transverse Ising chain and the reversed round-trip quench protocol.

is linearly ramped down and the system finally returns back to the classical Ising model, i.e., the limit of the ferromagnetic phase. In this limit, the kinks along the x axis play the role of defects and the number of defects $\mathcal{N}_F$ matches the number of excitations $\mathcal{N}$ exactly [23]:

$$\mathcal{N}_F \equiv \frac{1}{2}\sum_j \left(1 - \sigma_j^x \sigma_{j+1}^x\right) = \mathcal{N} \equiv \sum_q \eta_q^\dagger \eta_q. \quad (46)$$

In fact, the two definitions of the number of defects in the limit of paramagnetic phase $\mathcal{N}_P$ and the limit of ferromagnetic phase $\mathcal{N}_F$ are dual to each other. One can see this clearly by introducing the dual transformation [86] $\mu_j^z = \sigma_j^x \sigma_{j+1}^x$ and $\mu_j^x = \prod_{k<j} \sigma_k^z$, which leads to the mapping of defects,

$$\frac{1}{2}\sum_j \left(1 - \sigma_j^z\right) \leftrightarrow \frac{1}{2}\sum_j \left(1 - \mu_j^x \mu_{j+1}^x\right), \quad (47)$$

$$\frac{1}{2}\sum_j \left(1 - \sigma_j^x \sigma_{j+1}^x\right) \leftrightarrow \frac{1}{2}\sum_j \left(1 - \mu_j^z\right). \quad (48)$$

The followed calculations are direct and similar to previous ones. We will omit the details. In short, we get the same expressions of final excitation probability and density of defects as the ones in Eqs. (20) and (32). And the total dynamical phase ψ and the period of oscillation T_Q are the same as the ones in Eqs. (43) and (44), but note that we have $g_{rt} > g_c = 1$ now. We have also verified that the amplitude factor still falls into the asymptotical behavior $\lim_{\tau_Q \to \infty} M \sim (\ln \tau_Q)^{-3/2}$. However, if letting $g_{rt} \to \infty$, we get

$$\lim_{g_{rt} \to \infty} M = \sqrt{R}\left[\frac{\pi}{(1+R)(g_{rt}-1)}\right]^{3/2} \to 0, \quad (49)$$

which means the oscillation will fade out eventually as a dephasing effect. The oscillatory density of defects for $R = 1$ and $g_{rt} = 1.5$ is illustrated in Fig. 6.

III. QUANTUM XY CHAIN

The quantum XY chain with a transverse field reads as

$$H_{XY} = -\sum_{j=1}^N \left(J_x \sigma_j^x \sigma_{j+1}^x + J_y \sigma_j^y \sigma_{j+1}^y + g\sigma_j^z\right), \quad (50)$$

where $J_y (> 0)$ and $J_x (> 0)$ are interactions in x and y directions, respectively. We shall set J_x as an energy unit appropriately. The Hamiltonian can also be solved by Jordan-Wigner transformation [65,87]. As shown in Fig. 7, this model exhibits four phases: two ferromagnetic (FM) and two paramagnetic phases. One gets x-FM or y-FM phase if J_x or J_y prevails, respectively. In Fourier space, the quasiparticle dispersion reads as

$$\omega_q = 2\sqrt{\{g - (J_x + J_y)\cos q\}^2 + \{(J_x - J_y)\sin q\}^2}. \quad (51)$$

On the phase boundaries, the gap between the ground state and the lowest excited state vanishes at a critical quasimomentum q_c. The phase boundaries are three lines: $g = J_x + J_y$, $g = -J_x - J_y$, and $J_y = J_x$ with $q_c = 0, \pi$, and $\arccos(g/2J_x)$, respectively. Moreover, there are two tricritical points at $(g/J_x, J_y/J_x) = (\pm 2, 1)$.
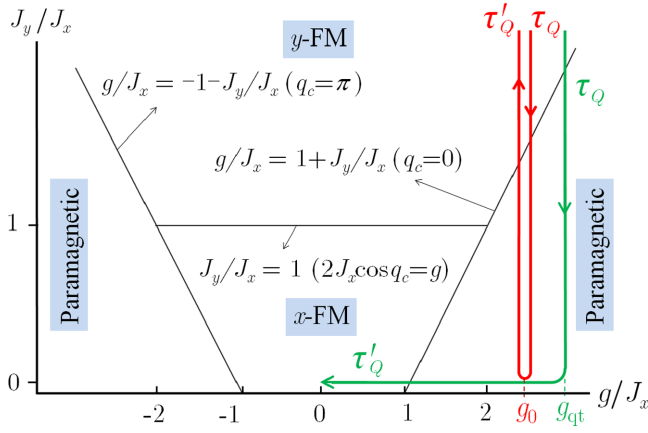
FIG. 7. Phase diagram of the quantum XY model and quench protocols. There are four phases divided by three phase boundaries. Two quench protocols are illustrated by the colored lines. In the round-trip quench protocol (red line), the starting and ending points are deeply located in the y-FM phase, and the turning point is set at $J_y/J_x = 0$. The system crosses over either one phase boundary twice ($0 < g_0 < 1$ and $g_0 \geqslant 2$) or two phase boundaries with each one twice ($1 < g_0 < 2$). In the quarter-turn quench protocol (green line), starting from the y-FM phase, the system goes across the phase boundary $g/J_x = 1 + J_y/J_x$ twice and finally reaches the limit of the x-FM phase, the classical Ising model. The turning point is labeled by the parameters fulfilling $g_{qt} > 1$ and $J_y/J_x = 0$. Please see more details in the text.

Aside from the round-trip quench protocol, another one, say *the quarter-turn quench protocol*, can also be applied to the quantum XY chain to produce the same kind of interference effect. We demonstrate them one by one.

A. Round-trip quench protocol

Without loss of generality, let us concentrate on the round-trip quench protocol depicted by the red line along the J_y/J_x direction as shown in Fig. 7. In this protocol, the parameter g_0/J_x is fixed and takes some appropriate value, the starting and ending points are located in the deep region of the y-FM phase, and the turning point is set at $J_y = 0$. In the following, we shall set the unit of energy, $J_x = 1$.

First, in the cases of $0 < g_0 < 1$ and $g_0 \geqslant 2$, the system crosses over the same phase boundary twice. We found that the density of defects still falls into the same formula as that expressed in Eq. (32), but the quantities in it behave differently depending on which phase boundary is crossed. We get

$$
n_0 =
\begin{cases}
\dfrac{\sqrt{2}}{\pi\left(4 - g_0^2\right)\sqrt{\tau_Q}} & (0 < g_0 < 1), \\[3mm]
\dfrac{1}{2\pi\left(g_0 - 2\right)\sqrt{2\tau_Q}} & (g_0 > 2), \\[3mm]
\dfrac{\Gamma(7/6)}{\pi\left(2\pi\tau_Q\right)^{1/6}} & (g_0 = 2),
\end{cases}
\tag{52}
$$

$$
f =
\begin{cases}
1 + \dfrac{1}{\sqrt{R}} - \dfrac{2}{\sqrt{1+R}} & (g_0 > 0 \wedge g_0 \neq 2), \\[3mm]
1 + \dfrac{1}{R^{1/6}} - \dfrac{2}{(1+R)^{1/6}} & (g_0 = 2),
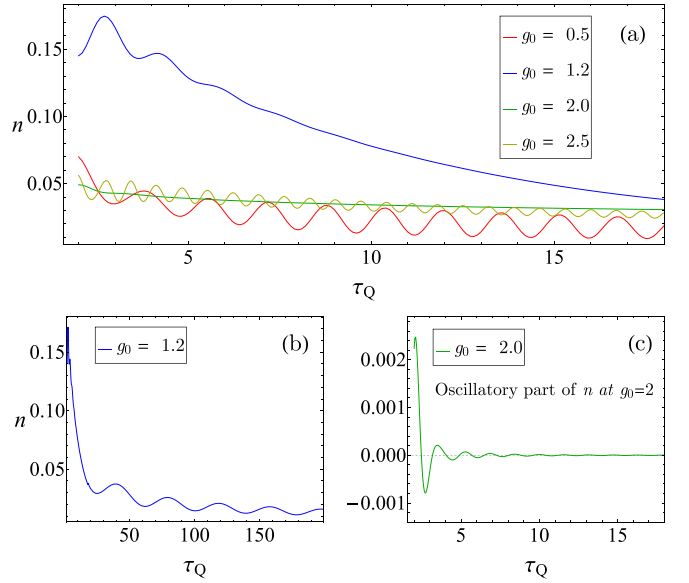\end{cases}
\tag{53}
$$

FIG. 8. (a) Density of defects n after the round-trip quench protocol is applied to the quantum XY chain. The parameters are $R = 1$ and $g_0 = 0.5$ (red line), 1.2 (blue line), 2.0 (green line), 2.5 (dark yellow line). (b) Density of defects n for $g_0 = 1.2$ in a larger range of τ_Q. (c) Oscillatory part of n for $g_0 = 2$. Please see more details in the text.

$$
T_Q =
\begin{cases}
\dfrac{\pi}{1 + R} & (0 < g_0 < 1), \\[3mm]
\dfrac{\pi}{(g_0 - 1)^2(1 + R)} & (g_0 \geqslant 2),
\end{cases}
\tag{54}
$$

and

$$
M \sim
\begin{cases}
e^{-\frac{g_0^2}{4 - g_0^2}\tau_Q} & (0 < g_0 < 1), \\[2mm]
(\ln \tau_Q)^{-3/2} & (g_0 > 2), \\[2mm]
\tau_Q^{-7/3} & (g_0 = 2).
\end{cases}
\tag{55}
$$

All the expressions have been verified by numerical solutions. δ is too tedious to be presented here since it is not important. As exemplified in Fig. 8(a), we see that M decreases exponentially in the case of $0 < g_0 < 1$, which is quite different from the case of $g_0 > 2$. At the tricritical point [$g_0 = 2$, see Figs. 8(a) and 8(c)], the factor n_0 behaves as $\sim\tau_Q^{-1/6}$, which is in agreement with the previous study [30]. And because M is a sum of a series of complex generalized hypergeometric functions in the case of $g_0 = 2$, we get a concise result $M \sim \tau_Q^{-7/3}$ by numerical fitting.

Second, in the case of $1 < g_0 < 2$, the system crosses over two phase boundaries with each one twice, which means that there are two independent sources of interferences because of two different critical quasimomenta, q_c's, corresponding to each phase boundary (see Fig. 7). Thus, the final defect density contains two kinds of oscillations since it is a sum of two contributions like

$$
n = n_0 \left\{ f + \sum_{i=1,2} M_i \cos\left(2\pi \frac{\tau_Q}{T_{Q,i}} + \delta_i\right) \right\},
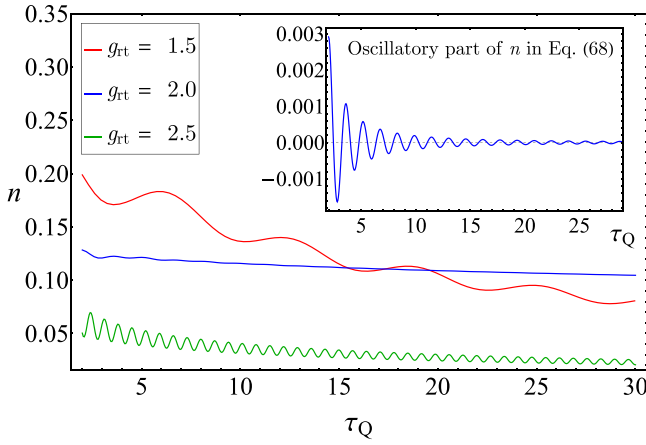\tag{56}
$$

FIG. 9. Density of defects n after the quarter-turn quench protocol is applied to the quantum XY chain. The parameters are $R = 1$ and $g_{qt} = 1.5$ (red line), 2 (blue line), 2.5 (green line). For the case of $g_{qt} = 2$ (blue line), the system goes across a tricritical point so that the result is expressed by Eq. (68), whose oscillatory part is illustrated in the inset.

where

$$n_0 = \frac{6 + g_0}{2\pi \left(4 - g_0^2\right)\sqrt{2\tau_Q}}, \tag{57}$$

$$f = 1 + \frac{1}{\sqrt{R}} - \frac{2}{\sqrt{1 + R}}, \tag{58}$$

$$T_{Q,1} = \frac{\pi}{1 + R}, \quad M_1 \sim e^{-\frac{g_0^2}{4 - g_0^2}\tau_Q}, \tag{59}$$

$$T_{Q,2} = \frac{\pi}{(g_0 - 1)^2(1 + R)}, \quad M_2 \sim (\ln \tau_Q)^{-3/2}. \tag{60}$$

The term with $T_{Q,1}$ and M_1 corresponds to the contribution due to the boundary $J_y/J_x = 1$, while the other term with $T_{Q,2}$ and M_2 corresponds to the contribution due to the boundary $g/J_x = 1 + J_y/J_x$. Since M_1 decreases exponentially with τ_Q increasing, the main contribution would come from the boundary $g/J_x = 1 + J_y/J_x$ for large enough τ_Q (say $\tau_Q \gtrsim 100$). The result is exemplified in Figs. 8(a) and 8(b).

B. Quarter-turn quench protocol

It is interesting to find new ways for realizing interference effect in the dynamics of this system since it contains more abundant phases and phase transitions. We propose another typical case, the quarter-turn quench protocol, which is shown in Fig. 9. The full procedure also contains two linear ramps and can be parametrized as

$$\begin{cases} J_y(t) = -\dfrac{t}{\tau_Q} \text{ and } g(t) = g_{qt} & (t_i < t \leqslant 0), \\ J_y(t) = 0 \text{ and } g(t) = g_{qt} - \dfrac{t}{\tau_Q'} & (0 < t \leqslant t_f), \end{cases} \tag{61}$$

where $t_i = -\infty$ and $t_f = g_{qt}\tau_Q'$. The starting point is set in the deep region of the y-FM phase. In the first stage, the interaction J_y is ramped down to zero so that the system is driven to the paramagnetic phase, which is ensued by the transverse field taking an appropriate value. Then, in the second stage, the transverse field is ramped down from $g_{qt} > 1$ to zero and

the system reaches the classical Ising model eventually. In this limit, again, the kinks along the x axis play the role of defects and the number of kinks matches the number of excitations exactly according to Eq. (46).

Because the situation is much more delicate, we shall omit the details of solution that is similar to the one elaborated in Sec. II A. Here we only write the final excitation probability before taking long-wave approximation

$$p_q^f = \begin{cases} A^2 + B^2 - 2AB \cos \psi & (1 < g_{qt} < 2), \\ A^2 + B^2 - 2AB \cos(\psi - \pi) & (g_{qt} \geqslant 2), \end{cases} \tag{62}$$

where

$$A = e^{-\pi \tau_Q (g_{qt} \sin q - \sin 2q)^2} \sqrt{1 - e^{-2\pi \tau_Q' \sin^2 q}}, \tag{63}$$

$$B = e^{-\pi \tau_Q' \sin^2 q} \sqrt{1 - e^{-2\pi \tau_Q (g_{qt} \sin q - \sin 2q)^2}}, \tag{64}$$

$$\begin{aligned} \psi = {}& \frac{\pi}{2} + 2(g_{qt} \cos q - \cos 2q)^2 \tau_Q + 2(g_{qt} - \cos q)^2 \tau_Q' \\ & + \tau_Q (g_{qt} \sin q - \sin 2q)^2 [\ln\{4\tau_Q (g_{qt} \cos q - \cos 2q)^2\} \\ & + \gamma_E] + \tau_Q' \sin^2 q [\ln\{4\tau_Q' (g_{qt} - \cos q)^2\} + \gamma_E]. \end{aligned} \tag{65}$$

The delicacy lies in the following facts.

First, the system undergoes two and three quantum phase transitions for $g_t > 2$ and $1 < g_t < 2$, respectively. In the former case, the two transitions occur at the same phase boundary $g = J_x + J_y$ with critical quasimomentum $q_c = 0$, thus, an oscillation in the density of defects would be observed inevitably. In the latter case, an extra transition occurs at the phase boundary $J_y/J_x = 1$ with critical quasimomentum $q_c = \arccos(g/2J_x)$, which is independent from the other two transitions and does not affect their interference. In both cases, the final density of defects still takes the general form in Eq. (32) but with renewed factor

$$f = \begin{cases} \dfrac{1}{g_{qt} - 2} + \dfrac{1}{\sqrt{R}} - \dfrac{2}{\sqrt{(g_{qt} - 2)^2 + R}} & (g_{qt} > 2), \\ \dfrac{6 + g_{qt}}{4 - g_{qt}^2} + \dfrac{1}{\sqrt{R}} - \dfrac{2}{\sqrt{(g_{qt} - 2)^2 + R}} & (1 < g_{qt} < 2), \end{cases} \tag{66}$$

and period of oscillation

$$T_Q = \frac{\pi}{(g_{qt} - 1)^2(1 + R)}. \tag{67}$$

We have also verified numerically that the amplitude of oscillation behaves asymptotically like $\lim_{\tau_Q \to \infty} M \sim (\ln \tau_Q)^{-3/2}$.

Second, if we let $g_{qt} = 2$, the system will go across a tricritical point in the first linear ramp and a usual critical point in the second linear ramp. It is well known that a single tricritical point will lead to a quite different scaling $n \sim \tau_Q^{-1/6}$ rather than the familiar scaling $n \sim \tau_Q^{-1/2}$, fit for the usual critical point. After the quarter-turn quench process, the final density of defects should contain both contributions intricately. Although no common QKZM factor [like n_0 in Eq. (30)] could be singled out, the final density of defect would reflect an interplay between the critical point and tricritical point.

Specifically, we arrive at

$$
n = \frac{\Gamma(7/6)}{\pi (2\pi \tau_Q)^{1/6}} + \frac{1}{2\pi \sqrt{2\tau_Q'}} - \frac{\pi^{1/3}\{\mathrm{Ai}(x)^2 + \mathrm{Bi}(x)^2\}}{\sqrt{2}(3\tau_Q)^{1/6}}
$$
$$
+ A' \cos\left(2\pi \frac{\tau_Q}{T_Q} + \delta\right), \tag{68}
$$

where $\mathrm{Ai}(x)$ and $\mathrm{Bi}(x)$ are two kinds Airy functions and $x = -\frac{\pi^{2/3}\tau_Q'}{(3\tau_Q)^{1/3}}$. The first two terms are individual contributions from two linear ramps, respectively. The third term is the nonoscillatory part of the interplay between the two ramps. The last term is the oscillatory part (please see the inset in Fig. 9), whose amplitude A' goes to zero quickly when τ_Q is large enough with the asymptotical behavior $\sim \tau_Q^{-3/2}$.

The final densities of defects for three distinct values of g_{qt} are illustrated in Fig. 9, in which the curves are obtained by integration on p_q^f expressed in Eq. (62) over the first Brillouin zone. And we have verified that a numerical solution of the dynamical TDBdG equations gives almost the same results. We can see that the oscillations for $g_{qt} \neq 2$ are prominent. While the oscillation for $g_{qt} = 2$ fades out very quickly with τ_Q increasing, although the period is still given by Eq. (67).

IV. DEFECT-DEFECT CORRELATOR WITH MULTIPLE LENGTH SCALES

In this section, we disclose an interesting phenomenon of multiple length scales, diagonal and off-diagonal ones, in the defect-defect correlator due to the interference effect. This correlator can reflect the special dephasing effect in the post-transition state. By a comparative study of the round-trip and reversed round-trip quench protocols for the transverse Ising chain, we show that the dephased result relies on how the diagonal and off-diagonal lengths are modulated by the controllable parameter in a quench protocol.

Throughout this paper, we are only concerned with two kinds of definitions of defects according to the destination of dynamics: $\mathcal{N}_P$ in Eq. (17) for the limit of paramagnetic phase and $\mathcal{N}_F$ in Eq. (46) for the limit of ferromagnetic phase. The former is fit for the round-trip quench protocol, while the latter the reversed round-trip quench protocol. Likewise, the defect-defect correlator should be defined differently for these two limits. For the round-trip quench protocol, it turns out to be the transverse spin-spin correlator

$$
C_r^{zz} = \langle \hat{P}_j \hat{P}_{j+r} \rangle - \langle \hat{P}_j \rangle \langle \hat{P}_{j+r} \rangle
$$
$$
= \frac{1}{4}\left(\langle \sigma_j^z \sigma_{j+r}^z \rangle - \langle \sigma_j^z \rangle \langle \sigma_{j+r}^z \rangle\right), \tag{69}
$$

where the defect operator $\hat{P}_j = \frac{1}{2}(1 - \sigma_j^z)$. While for the reversed round-quench protocol, it is the kink-kink correlator [48]

$$
C_r^{\mathrm{KK}} = \langle \hat{F}_j \hat{F}_{j+r} \rangle - \langle \hat{F}_j \rangle \langle \hat{F}_{j+r} \rangle, \tag{70}
$$

where the defect (or kink) operator $\hat{F}_j = \frac{1}{2}(1 - \sigma_j^x \sigma_{j+1}^x)$.

A. Transverse spin-spin correlator for the round-trip quench protocol

We consider the round-trip quench protocol applied to the transverse Ising chain first. For abbreviation, we confine our discussion to the simplest case with $R = 1$ and $g_{\mathrm{rt}} = 0$.

1. Fermionic correlators and multiple length scales

The system goes back to the paramagnetic phase finally, thus the transverse correlator plays the role of defect-defect correlation. The details on computing this correlator are presented in Appendix B. Here we only quote the result:

$$
C_r^{zz} = |\beta_r|^2 - \alpha_r^2, \tag{71}
$$

where

$$
\alpha_r \equiv \langle c_j^+ c_{j+r} \rangle = -\int_0^\pi \frac{dq}{\pi} |v_q(t_f)|^2 \cos(qr), \tag{72}
$$

$$
\beta_r \equiv \langle c_j c_{j+r} \rangle = \int_0^\pi \frac{dq}{\pi} u_q(t_f) v_q^*(t_f) \sin(qr) \tag{73}
$$

are diagonal and off-diagonal quadratic fermionic correlators [28]. The negative term in Eq. (71) implies an antibunching effect of the defects in short space distances, which means the defects can hardly approach one another.

For the diagonal fermionic correlator α_r, we arrive at

$$
\alpha_r = \frac{2e^{-r^2/\hat{\xi}^2}}{\sqrt{\pi}\,\hat{\xi}}\left(1 - \sqrt{2}e^{-r^2/\hat{\xi}^2}\right)
$$
$$
+ \sum_{m=1,2} \frac{\sqrt{8}(-1)^m e^{-r^2/(l_m^\alpha)^2}}{(2m\pi^2)^{1/4}\sqrt{\hat{\xi}\,l_m^\alpha}} \sin\phi_{m,r}^\alpha, \tag{74}
$$

where

$$
\phi_{m,r}^\alpha = 4\tau_Q - \frac{b}{m}\frac{r^2}{(l_m^\alpha)^2} + \frac{1}{2}\arctan\frac{b}{m} \tag{75}
$$

are phase factors with $b = \frac{1}{\pi}\{\ln(4\tau_Q) + \gamma_E - 2\} \approx \frac{\ln \tau_Q}{\pi}$ and

$$
\hat{\xi} = 4\sqrt{\pi \tau_Q}, \tag{76}
$$

$$
l_m'^\alpha = 2\sqrt{2m\pi \tau_Q}\sqrt{1 + \left(\frac{b}{m}\right)^2} \tag{77}
$$

are three length scales. Exposed by the interference, $l_m^{\alpha's}$ ($m = 1, 2$) are two new lengths that could be called the *diagonal lengths* since they appear in the diagonal fermionic correlator. They attenuate the sinusoidal interference terms $\sin\phi_{m,r^{\alpha's}}$ by the Gaussian decaying factors in space. We still call $\hat{\xi}$ the *KZ length*, although it also appears in the diagonal fermionic correlator.

For the off-diagonal fermionic correlator β_r, we arrive at

$$
\beta_r = \sum_{m=1}^5 (-1)^{m-1}\frac{y_m r}{\sqrt{\hat{\xi}\,(l_m^\beta)^3}}e^{-r^2/(l_m^\beta)^2}e^{i\phi_m^\beta(r)}, \tag{78}
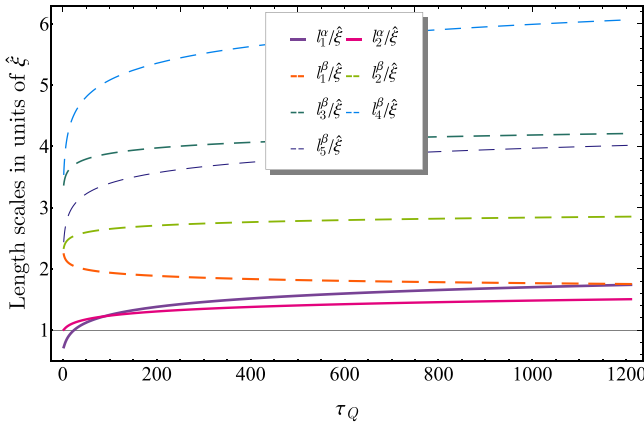$$

FIG. 10. Length scales l_m^α ($m = 1, 2$) and l_m^β ($m = 1, \dots, 5$), in the transverse spin-spin correlator. All length scales are plotted in units of KZ length $\hat{\xi}$. We have fixed the parameters $R = 1$ and $g_f = 10$.

where $y_m = \frac{2Y_m}{\{\pi^2(h_m)^3\}^{1/4}}$ are coefficients with $Y_2 = \sqrt{\frac{e}{\ln 2}}$ for $m = 2$ and $Y_m = \frac{1}{2}\sqrt{\frac{e}{\ln 2}}$ for other m,

$$\phi_m^\beta(r) = \lambda_m' - \frac{\lambda_m r^2}{\pi h_m (l_m^\beta)^2} - \frac{3}{2} \arg\left(1 - i\frac{\lambda_m}{\pi h_m}\right) \qquad (79)$$

are phase factors with

$$\lambda_1 = \ln \tau_Q - 2g_f - 2\ln(g_f - 1),$$
$$\lambda_2 = \lambda_3 = -\ln \tau_Q - 2g_f - 2\ln(g_f - 1),$$
$$\lambda_4 = \lambda_5 = -3\ln \tau_Q - 2g_f - 2\ln(g_f - 1),$$
$$\lambda_1' = -\lambda_2' = -\lambda_3' = \frac{\pi}{4} + 2\tau_Q,$$
$$\lambda_4' = \lambda_5' = -\frac{3\pi}{4} - 6\tau_Q,$$
$$h_1 = h_2 = h_5 = 2 + \frac{1}{\ln 2}, \; h_3 = h_4 = \frac{1}{\ln 2},$$

and

$$l_m^\beta = 2\sqrt{\pi h_m \tau_Q}\sqrt{1 + \left(\frac{\lambda_m}{\pi h_m}\right)^2} \qquad (80)$$

are other five new lengths. Likewise, we call them *off-diagonal lengths*.

So we get eight lengths in total. We illustrate them in Fig. 10 by setting the typical parameters $R = 1$ and $g_f = 10$. It is clear to see that $l_{m\beta's}$ are larger than $l_m^{\alpha's}$ and l_4^β is always the largest one overall. In fact, except for the KZ length ($\hat{\xi} \sim \sqrt{\tau_Q}$), all other lengths share the same asymptotic behavior $\sim\sqrt{\tau_Q}\ln \tau_Q$ for a fixed finite value of g_f.

The transverse spin-spin correlator scaled as $n_0^{-2}C_r^{zz}$ versus the scaled distance $n_0 r$ is exemplified in Fig. 11. We see that the length scales coming out of the diagonal and off-diagonal fermionic correlators play quite different roles. The transverse correlator is governed by the diagonal part for small space distances and by the off-diagonal part for large space distances,
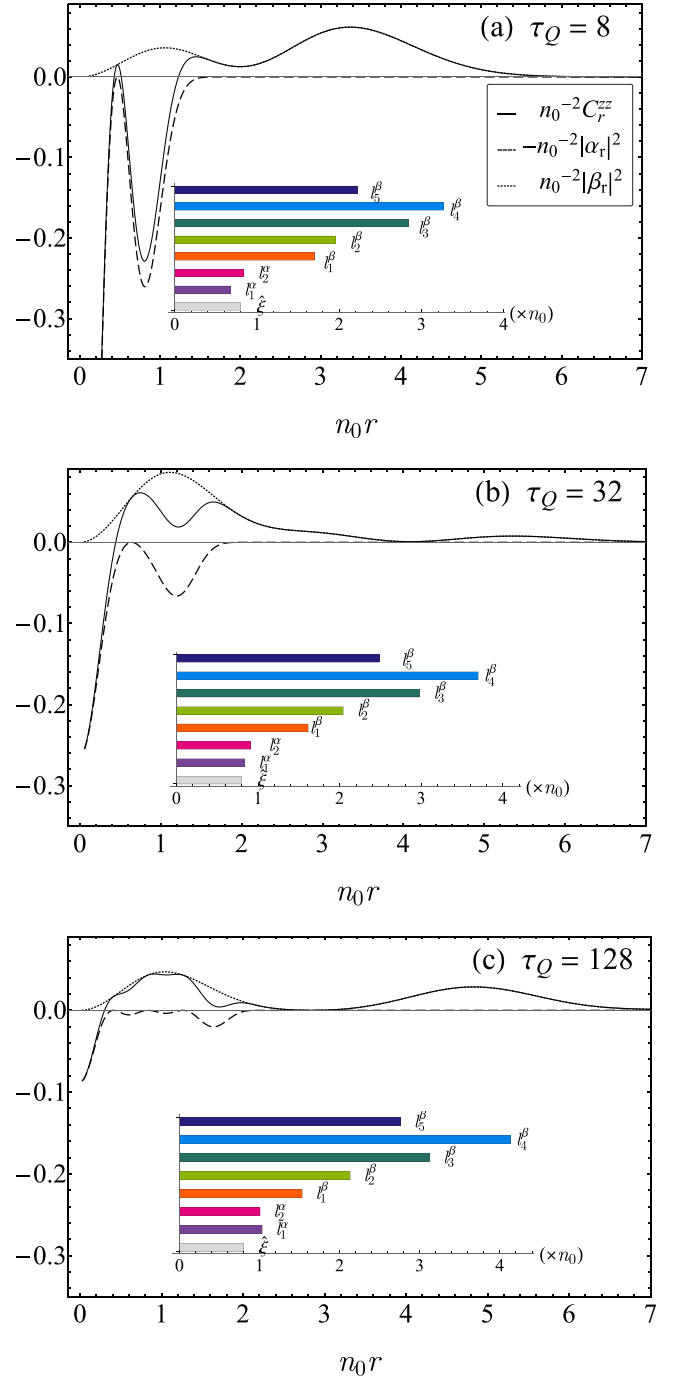

FIG. 11. Transverse spin-spin and fermionic correlators. The correlators C_r^{zz}, $-|\alpha_r|^2$, and $|\beta_r|^2$ scaled in n_0^2 are plotted versus the rescaled distance $n_0 r$ for (a) $\tau_Q = 8$, (b) $\tau_Q = 32$, and (c) $\tau_Q = 128$. Other parameters are $R = 1$ and $g_f = 10$. The multiple lengths are illustrated by the colored bar charts in each inset. The fermionic correlator $-|\alpha_r|^2$ also stands for the dephased transverse spin-spin correlator when $g_f \to \infty$ according to Eq. (89).

i.e., we have

$$C_r^{zz} \approx \begin{cases} -\alpha_r^2 & [r \ll \min(l_m^\alpha, \hat{\xi})], \\ |\beta_r|^2 & [r \gtrsim \min(l_m^\beta)], \end{cases} \qquad (81)$$
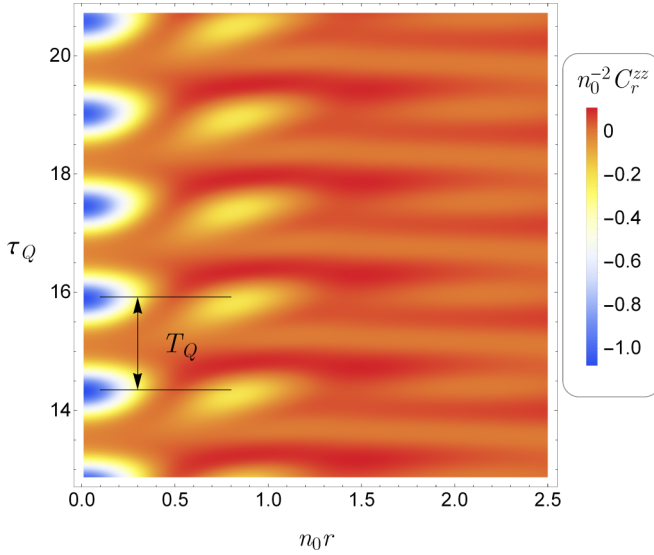
FIG. 12. Density plot of $n_0^{-2}C_r^{zz}$ in typical ranges of variables $n_0 r$ and τ_Q. We have set the parameters $R = 1$ and $g_f = 10$. $T_Q = \frac{\pi}{2}$ denotes the period of the oscillation along the direction of the variable τ_Q in the transverse spin-spin correlator.

approximately. The former is due to the fact $(l_m^\alpha)^{-1/2} \gg r(l_m^\beta)^{-3/2}$ for small r, and the latter $e^{-(l_m^\beta/l_m^\alpha)^2} \to 0$ and $e^{-(l_m^\beta/\hat{\xi})^2} \to 0$ for large enough r. When the space distance exceeds the largest length scale, i.e., $r > l_4^\beta$, the transverse correlator reduces to the Maxwell-Boltzmann form

$$C_r^{zz} \approx \frac{1}{16}\sqrt{\frac{e^2 \ln 2}{\pi}}\frac{r^2}{\hat{\xi}\left(l_4^\beta\right)^3}e^{-2r^2/\left(l_4^\beta\right)^2} \qquad (82)$$

with only one prevailing length l_4^β. While for intermediate space distances, the transverse correlator is influenced by all lengths.

2. Periodicity due to interference

Both fermionic correlators α_r and β_r contain interference terms. It is easy to discern an oscillation with a period $T_Q = \frac{\pi}{2}$ (please note that $R = 1$ at present), in the diagonal part of the transverse spin-spin correlator, $-|\alpha_r|^2$, along the τ_Q direction. While for the off-diagonal part $|\beta_r|^2$, one can find that

$$|\beta_r|^2 \sim \sum_{m,n=1...5} A_{mn}\cos(\Omega_{mn}\tau_Q + \delta_{mn}), \qquad (83)$$

where

$$\Omega_{mn} \equiv \frac{\lambda_m' - \lambda_n'}{\tau_Q} - \frac{r^2}{\tau_Q^2}\left(\frac{1}{\lambda_m} - \frac{1}{\lambda_n}\right)$$
$$- \frac{3}{2\tau_Q}\left[\arg\left(1 - i\frac{\lambda_m}{\pi h_m}\right) - \arg\left(1 - i\frac{\lambda_n}{\pi h_n}\right)\right]. \qquad (84)$$

Ω_{mn} takes two possible values, 4 or 8, asymptotically when $\tau_Q \gg r$ (please note that we also have $\tau_Q \gg \hat{\xi}, l_m^\beta$). Thus, the fermionic correlator $|\beta_r|^2$ also exhibits the same period $T_Q = \frac{\pi}{2}$. The oscillatory behavior characterized by the period T_Q can be easily observed in the density plot of the full transverse spin-spin correlator as shown Fig. 12.

3. Quantum dephasing

In Sec. II B 2, we saw the interplay between the interference and the quantum dephasing results in the oscillation of the density of defects. Now, we reveal that the phenomenon of multiple length scales is also a consequence of this interplay.

Here the off-diagonal lengths $l_{m\beta's}$ rely on the controllable parameter g_f. If we let $g_f \gg \ln \tau_Q$, instead of fixing g_f, all off-diagonal lengths will grow linearly with the final time $t_f = g_f\tau_Q$ increasing,

$$l_m^\beta \sim \sqrt{\tau_Q}g_f = \frac{t_f}{\sqrt{\tau_Q}}. \qquad (85)$$

The off-diagonal fermionic correlator can be written as

$$\beta_r = \int_0^\pi \frac{dq}{\pi}\sin(qr)e^{-h_m\pi\tau_Q q^2}X_m\sqrt{2\pi\tau_Q}$$
$$\times e^{i\left(4t_f - 2\frac{t_f^2}{\tau_Q} + 2q^2 t_f\right)}\left(\sum_{m=1}^5 (-1)^{m-1}e^{i\lambda_m'}\right). \qquad (86)$$

We see the off-diagonal lengths $l_m^{\beta's}$ play the role of dephasing length because the phase factor $e^{i(4t_f - 2\frac{t_f^2}{\tau_Q} + 2q^2 t_f)}$ oscillates very rapidly with the quasimomentum q varying and the magnitude of β_r becomes negligible when $t_f \to \infty$. The dephasing time t_D measures the time when the dephasing effect becomes noticeable [48]. Here, it can be estimated by setting

$$\frac{\lambda_m}{\pi h_m} = 1 \qquad (87)$$

in Eq. (80). Now that we have leading terms linear in g_f, i.e., $|\lambda_m| \propto 2g_f = 2\frac{t_f}{\tau_Q}$, and there are two values of h_m (i.e., $h_1 = h_2 = h_5 = 2 + \frac{1}{\ln 2}$ and $h_3 = h_4 = \frac{1}{\ln 2}$), we get two dephasing times due to the multiple length scales

$$t_D^{3,4} = \frac{1}{2\ln 2}\pi\tau_Q,$$
$$t_D^{1,2,5} = \left(1 + \frac{1}{2\ln 2}\right)\pi\tau_Q, \qquad (88)$$

which means that the off-diagonal fermionic correlator decreases significantly at two moments with t_f increasing. For long enough evolution time ($t_f \gg t_D$), the off-diagonal fermionic correlator will be suppressed. Physically, this is due to the fact that the excited quasiparticle modes are completely dephased. Meanwhile, the KZ length and the two diagonal lengths remain intact after such a dephasing, which leads to a reduced transverse spin-spin correlator

$$C_r^{zz}(t_f \to \infty) \approx -\alpha_r^2. \qquad (89)$$

This result is illustrated by the dashed lines in Fig. 11. Aside from the strong antibunching, the dashed lines also display a sinusoidal behavior that is rendered by the diagonal lengths. The sinusoidal behavior is in contrast to the traditional case without interference, where only the KZ length remains [48]. Moreover, the periodicity in τ_Q direction still remains in the dephased correlator.

B. Kink-kink correlator for the reversed round-trip quench protocol

Now we point out that the same phenomenon of multiple length scales will also appear in the kink-kink correlator in the reversed round-trip quench protocol applied to the transverse Ising chain. But, there are some interesting differences that need to be addressed adequately. We mainly focus on the dephasing effect that is regulated by the multiple lengths.

The kink-kink correlator after the reverse round-trip quench process can still be reduced to

$$C_r^{\text{KK}} = |\beta_r'|^2 - (\alpha_r')^2, \tag{90}$$

where α_r' and β_r' are diagonal and off-diagonal quadratic fermionic correlators. For the diagonal fermionic correlator α_r', we arrive at

$$\alpha_r' = \frac{2e^{-r^2/\hat{\xi}^2}}{\sqrt{\pi}\,\hat{\xi}}\left(1 - \sqrt{2}e^{-r^2/\hat{\xi}^2}\right) + \sum_{m=1,2}\frac{\sqrt{8}(-1)^m e^{-r^2/(l_m'^{\alpha})^2}}{(2m\pi^2)^{1/4}\sqrt{\hat{\xi}\,l_m'^{\alpha}}}\sin\phi_{m,r}'^{\alpha}, \tag{91}$$

where

$$\phi_{m,r}'^{\alpha} = 4\tau_Q - \frac{b'}{m}\frac{r^2}{\left(l_m'^{\alpha}\right)^2} + \frac{1}{2}\arctan\frac{b'}{m} \tag{92}$$

are phase factors with

$$b' = 2[\ln\{4\tau_Q(g_{\text{rt}} - 1)^2\} + 2(g_{\text{rt}} - 1) + \gamma_E], \tag{93}$$

$$l_m'^{\alpha} = \frac{1}{\pi}\sqrt{2m\pi\tau_Q}\sqrt{1 + \left(\frac{b'}{m}\right)^2}\quad(m = 1, 2) \tag{94}$$

and $\hat{\xi}$ defined in Eq. (76) is the usual KZ length.

For the off-diagonal fermionic correlator β_r', we arrive at

$$\beta_r' = \sum_{m=1}^{5}(-1)^{m-1}\frac{y_m\,r}{\sqrt{\hat{\xi}\left(l_m'^{\beta}\right)^3}}e^{-r^2/\left(l_m'^{\beta}\right)^2}e^{i\phi_m'^{\beta}(r)}, \tag{95}$$

$y_m = \frac{2Y_m}{[\pi(h_m)^3]^{1/4}}$ are coefficients with $Y_2 = \sqrt{\frac{e}{\ln 2}}$ for $m = 2$ and $Y_m = \frac{1}{2}\sqrt{\frac{e}{\ln 2}}$ for other values of m,

$$\phi_m'^{\beta}(r) = \chi_m' - \frac{\chi_m r^2}{\pi h_m(l_m^{\beta})^2} - \frac{3}{2}\arg\left(1 - i\frac{\chi_m}{\pi h_m}\right) \tag{96}$$

are phase factors with

$$\chi_1 = \ln 4\tau_Q + 4g_{\text{rt}} - 2 + 4\ln(g_{\text{rt}} - 1) + \gamma_E,$$

$$\chi_{2/3} = -(\ln 4\tau_Q - 2 + \gamma_E),$$

$$\chi_{4/5} = -\{3\ln 4\tau_Q + 4g_{\text{rt}} - 6 + 4\ln(g_{\text{rt}} - 1) + 3\gamma_E\},$$

$$\chi_1' = \frac{\pi}{4} + 2\tau_Q(2g_{\text{rt}}^2 - 4g_{\text{rt}} + 1),$$

$$\chi_{2/3}' = -\frac{\pi}{4} - 2\tau_Q,$$

$$\chi_{4/5}' = -\frac{3\pi}{4} - 2\tau_Q(2g_{\text{rt}}^2 - 4g_{\text{rt}} + 3),$$

$$h_1 = h_2 = h_5 = 2 + \frac{1}{\ln 2},\quad h_3 = h_4 = \frac{1}{\ln 2},$$

and

$$l_m'^{\beta} = 2\sqrt{\pi h_m \tau_Q}\sqrt{1 + \left(\frac{\chi_m}{\pi h_m}\right)^2} \tag{97}$$

are five more new length scales.

The dephasing process here is quite different from the former of the transverse spin-spin correlator. Now we notice the fact that the KZ length $\hat{\xi}$ and the off-diagonal lengths l_2^{β} and l_3^{β} are free of g_{rt}, while all others increase linearly in g_{rt}: $l_{1/2}'^{\alpha}, l_{1/4/5}'^{\beta} \sim \sqrt{\tau_Q}g_{\text{rt}}$. This fact means that only $\hat{\xi}$, l_2^{β}, and l_3^{β} can remain intact with the parameter $g_{\text{rt}} \to \infty$. So, after such a dephasing, we get a reduced kink-kink correlator

$$C_r^{\text{KK}}(g_{\text{rt}} \to \infty) = -\frac{4e^{-2r^2/\hat{\xi}^2}}{\pi\,\hat{\xi}^2}(1 - \sqrt{2}e^{-r^2/\hat{\xi}^2})^2 + \left|\sum_{m=2,3}\frac{(-1)^{m-1}y_m\,r\,e^{-r^2/\left(l_m'^{\beta}\right)^2}e^{i\phi_m'^{\beta}(r)}}{\sqrt{\hat{\xi}\left(l_m'^{\beta}\right)^3}}\right|^2. \tag{98}$$

These dephased kink-kink correlators for $\tau_Q = 8$, 32, 128 are illustrated by the red dashed lines in Fig. 13, which are plotted in comparison with the kink-kink correlators with finite value of $g_{\text{rt}} = 10$ (black lines). We can still observe the strong antibunching in short space distances. But the sinusoidal behavior is rendered by the off-diagonal lengths instead of the diagonal ones. More interestingly, despite a bit of oscillatory behavior, the dephased kink-kink correlator can even become positive due to the contributions of the two off-diagonal lengths l_2^{β} and l_3^{β}.

V. SUMMARY AND DISCUSSION

In summary, we have demonstrated a kind of concise interference effect by applying appropriately designed quench protocols to the transverse Ising and quantum XY models. The underlying mechanism can be well described by the combination of two successive Landau-Zener transitions, which renders an exposure of the dynamical phase in the final excitation probability so that the characteristic lengths in it are embedded in the density of defects. In essence, the density of defects can reflect the interference between two same or different critical dynamics in a neat way. Let us retrospect a typical one as shown in Eq. (68): its first two terms are individual contributions of the two critical dynamics and the rest two terms are joint contributions, in which one is nonoscillatory and the other oscillatory. On the practical side, the interference effect can be directly observed by the coherent many-body oscillation in the density of defects with characteristic period T_Q. As we discovered for several typical quench protocols, the characteristic period T_Q falls into a generic form, say, e.g., Eqs. (44), (54), and (67). We expect it is waiting to be confirmed or generalized in other systems. The period comes from the term proportional to $\tau_Q + \tau_Q' = (1 + R)\tau_Q$ in the dynamical phase [e.g., Eqs. (23), (43), and (65)]. In the dynamical phase, another term proportional to $(q - q_c)^2$ also plays important roles. First, it affects the amplitude of oscillation in the density of defects. Second, it can lead to
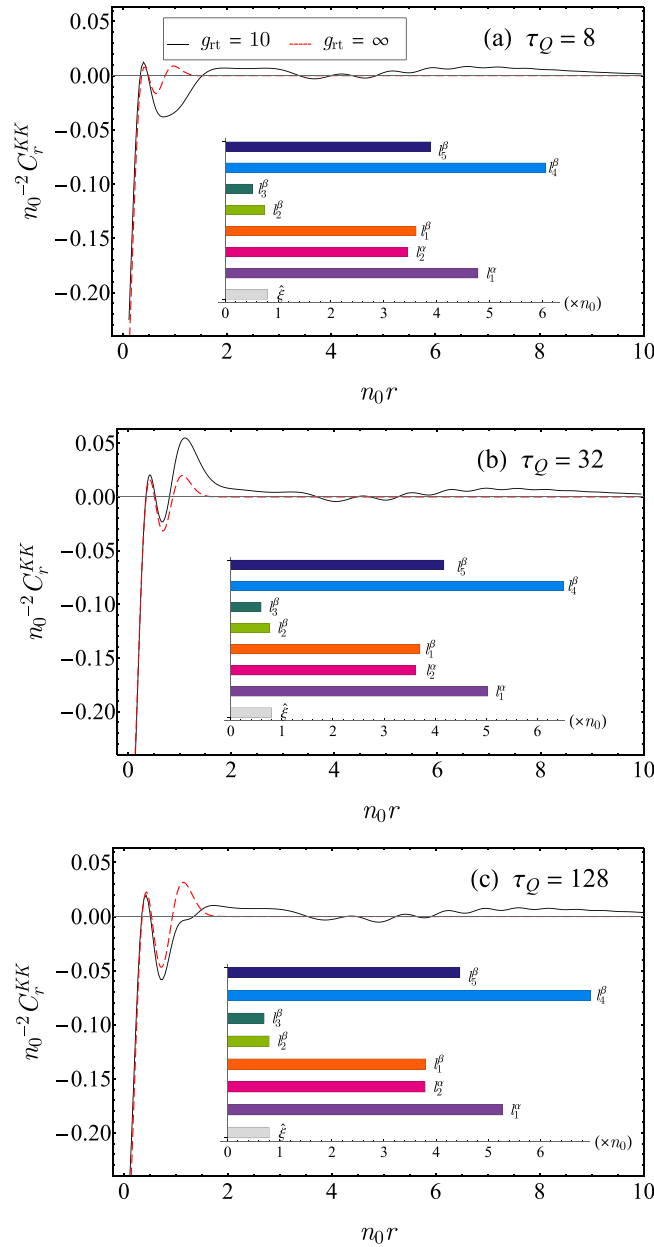
FIG. 13. Kink-kink correlator C_r^{KK} scaled in n_0^2 versus rescaled distance $n_0 r$ for $\tau_Q = 8$ (a) 32 (b) and 128 (c). The black solid lines and the colored bar charts of multiple lengths in the insets are for the case of $g_{rt} = 10$. The red dashed lines are dephased results for $g_{rt} \to \infty$.

the phenomenon of multiple length scales in the defect-defect correlator.

In an actual quench process, the control over the system is not so perfect that the interference effect would have to be potentially impacted by decoherence, noise, flaws, and so on. These important topics need to be studied further in the future [88–92]. In view of the current technological advances, e.g., the experiment in which a transverse Ising chain was emulated by Rydberg atoms [59], or other ones that pave the way to study quantum dynamics [93–96], the interferometry proposed in this paper may provide a valuable means used as a diagnostic tool to benchmark the experimental implemen-

tations of emulation against loss of coherence. For example, the interference may be utilized in a quantum heat engine to evaluate whether the working medium has fully reached a steady state with maximum entropy or ground state and to estimate an optimal time for the working medium to be thermalized or cooled [97].

APPENDIX A: SOLUTION OF THE LANDAU-ZENER PROBLEM WITH INTERFERENCE

In this Appendix, we give the solution of the TDBdG equations in Eq. (16), which was deduced for the round-trip quench protocol applied to the transverse Ising chain. We also work out the final excitation probability p_q^f and the density of defects n. We discuss the case of $g_{rt} = 0$ in detail first, then the cases of $0 < g_{rt} < 1$ and $g_{rt} = 1$ briefly.

1. Solution for $g_{rt} = 0$

a. First stage: Linear ramp from $g_i \gg 1$ to $g_{rt} = 0$

In the first stage, we can think the time t varies from $t_i = -\infty$ to 0. The TDBdG equations in Eq. (16) can be mapped to the standard Landau-Zener problem [98,99] and the solution can be expressed in terms of complex parabolic cylinder functions $D_\nu(z)$ as

$$v_q(z) = C_1 D_{-s_q-1}(iz) + C_2 D_{-s_q-1}(-iz), \quad (A1)$$

$$u_q(z) = \frac{e^{i\pi/4}}{\sqrt{\tau_Q} \sin q}\left(i\frac{d}{dz} + \frac{iz}{2}\right)v_q(z)$$

$$= \frac{(-1)^{1/4}}{\sqrt{\tau_Q} \sin q}\{C_1 D_{-s_q}(iz) - C_2 D_{-s_q}(-iz)\}, \quad (A2)$$

where $z = 2\sqrt{\tau_Q}(\frac{t}{\tau_Q} + \cos q)e^{i\pi/4}$, $s_q = -i\tau_Q \sin^2 q$, and both C_1 and C_2 are normalization coefficients. By the initial conditions $u_q(-\infty) = 1$ and $v_q(-\infty) = 0$, we find the values of the two normalization coefficients

$$C_1 = \frac{e^{-i\pi/4}\sqrt{\tau_Q} \sin q}{D_{-s_q}(iz)}\bigg|_{t\to t_i=-\infty}, \quad C_2 = 0. \quad (A3)$$

b. Second stage: Linear ramp from $g_{rt} = 0$ to $g_f \gg 1$

In the second stage, we assume the time t varies from 0 to $\frac{t_f}{\tau_Q'} \gg 1$. The basic TDBdG equations are the same as the ones in Eq. (16). Likewise, the solution is

$$u_q(w) = C_1' D_{-s_q'-1}(iw) + C_2' D_{-s_q'-1}(-iw), \quad (A4)$$

$$v_q(w) = \frac{e^{i\pi/4}}{\sqrt{\tau_Q'} \sin q}\left(i\frac{d}{dw} + \frac{iw}{2}\right)u_q'(w), \quad (A5)$$

where $w = -2\sqrt{\tau'_Q}(-\frac{t}{\tau'_Q} + \cos q)e^{i\pi/4}$, $s'_q = -i\tau'_Q \sin^2 q$, and C'_1 and C'_2 both are normalization coefficients. The two normalization coefficients read as

$$C'_1 = \frac{D_{-s'_q}(-iw_0)u^0_q + \frac{v^0_q\sqrt{\tau'_Q}\sin q}{(-1)^{1/4}}D_{-s'_q-1}(-iw_0)}{de(s'_q, w_0)}, \quad (A6)$$

$$C'_2 = \frac{D_{-s'_q}(iw_0)u^0_q - \frac{v^0_q\sqrt{\tau'_Q}\sin q}{(-1)^{1/4}}D_{-s'_q-1}(iw_0)}{de(s'_q, w_0)}, \quad (A7)$$

where $w_0 = w|_{t\to 0}$ and the denominator of $C'_{1/2}$ is

$$de(s'_q, w_0) = \sum_{\alpha=\pm} D_{-s'_q-1}(-i\alpha w_0)D_{-s'_q}(i\alpha w_0). \quad (A8)$$

c. Asymptotic analysis of the solutions

To reduce the above rigorous solution with elementary functions, we need to apply the asymptotes of $D_m(z)$ that are given by [99]

$$D_m(z) = e^{-z^2/4}z^m, \quad \forall \, |\arg(z)| < 3\pi/4, \quad (A9)$$

$$D_m(z) = e^{-z^2/4}z^m - \frac{\sqrt{2\pi}}{\Gamma(-m)}e^{-im\pi}e^{z^2/4}z^{-m-1},$$

$$\forall \, -5\pi/4 < \arg(z) < -\pi/4. \quad (A10)$$

We concern the asymptotic solution at two moments: (1) $t = 0$ (the end of the first stage), (2) $t = t_f$ (the end of the second stage).

At $t = 0$, the solution valid for $q \lesssim \frac{1}{\sqrt{\pi\tau_Q}}$ is reduced to

$$u^0_q \equiv u_q(0) = \frac{C_1}{\sqrt{\tau_Q}\sin q}e^{-3\pi\tau_Q\sin^2 q/4}e^{i\theta^u_q}, \quad (A11)$$

$$v^0_q \equiv v_q(0) = \frac{C_1\text{sgn}(q)\sqrt{2\pi}}{|\Gamma(1+s_q)|}e^{-\pi\tau_Q\sin^2 q/4}e^{-i\theta^v_q}, \quad (A12)$$

where coefficient C_1 fulfills

$$|C_1|^2 = \tau_Q \sin^2 q \, e^{-\pi\tau_Q\sin^2 q/2}, \quad (A13)$$

and the two phase angles are

$$\theta^u_q = \tau_Q \cos^2 q + \frac{\tau_Q \sin^2 q}{2}\ln(4\tau_Q) + \arg\{\Gamma(1+s_q)\}, \quad (A14)$$

$$\theta^v_q = \frac{\pi}{4} + \tau_Q \cos^2 q + \frac{\tau_Q \sin^2 q}{2}\ln(4\tau_Q), \quad (A15)$$

$\Gamma(x)$ is the gamma function, $\frac{\sqrt{2\pi}}{|\Gamma(1+ix)|} = \sqrt{2\sinh(\pi x)/x}$, and $\arg\{\Gamma(1+ix)\} \approx -\gamma_E x$ with Euler constant $\gamma_E \approx 0.577216$. Please notice that the initial conditions in the second stage are exactly Eqs. (A11) and (A12).

At $t = t_f$, the solution is reduced to

$$u_q(t_f) = \sqrt{(1 - e^{-2\pi\tau'_Q\sin^2 q})(1 - e^{-2\pi\tau_Q\sin^2 q})}e^{-i(\theta^v_q+\phi^a_q)}$$
$$+ e^{-\pi\tau_Q\sin^2 q}e^{-\pi\tau'_Q\sin^2 q}e^{i(\theta^u_q-\phi^b_q)}, \quad (A16)$$

$$v_q(t_f) = -e^{-\pi\tau_Q\sin^2 q}\sqrt{1 - e^{-2\pi\tau'_Q\sin^2 q}}e^{i(\theta^u_q+\phi^a_q)}$$
$$+ e^{-\pi\tau'_Q\sin^2 q}\sqrt{1 - e^{-2\pi\tau_Q\sin^2 q}}e^{-i(\theta^v_q-\phi^b_q)}, \quad (A17)$$

where $\theta^{u/v}_q$ are to be found in Eqs. (A14) and (A15) and

$$\phi^a_q = \frac{\pi}{4} + \tau'_Q\{(g_f - \cos q)^2 + \cos^2 q\} + \arg\{\Gamma(1+s'_q)\}$$
$$+ \tau'_Q \sin^2 q \, \ln\{4\tau'_Q(g_f - \cos q)\cos q\}, \quad (A18)$$

$$\phi^b_q = \tau'_Q\{(g_f - \cos q)^2 - \cos^2 q\} + \tau'_Q \sin^2 q \, \ln\frac{g_f - \cos q}{\cos q} \quad (A19)$$

are another two phase angles produced by the second stage of the quench process.

By Eq. (18), we can deduce the final excitation probability as

$$p^f_q = |v_q(t_f)u_q - u_q(t_f)v_q|^2$$
$$= |-A\,e^{i(\theta^u_q+\phi^a_q)} + B\,e^{-i(\theta^v_q-\phi^b_q)}|^2$$
$$= A^2 + B^2 - 2AB\cos\psi, \quad (A20)$$

where $u_q \approx 1$ and $v_q \approx 0$ are the equilibrium Bogoliubov amplitudes defined in Eq. (10) at $g = g_f \gg 1$. A, B, and ψ are defined in Eqs. (21), (22), and (23) in the main text.

The density of defects is defined in Eq. (19). In the thermodynamical limit $N \to \infty$, we can replace the sum with an integral

$$n = \int_0^\pi \frac{dq}{\pi}p_q. \quad (A21)$$

First, we make an approximation

$$\sqrt{(1 - e^{-2\pi\tau_Q q^2})(1 - e^{-2\pi R\tau_Q q^2})}$$
$$\approx \frac{1}{2}\left[\sqrt{R}(1 - e^{-2\pi\tau_Q q^2}) + \sqrt{\frac{1}{R}}(1 - e^{-2\pi R\tau_Q q^2})\right]. \quad (A22)$$

Then, the defect density can be worked out by the integral formula

$$\int_0^\pi \frac{dq}{\pi}e^{-cq^2}\cos(a + bq^2) = \frac{\cos\left[a + \frac{\pi}{4} - \frac{1}{2}\arctan(c/b)\right]}{2\sqrt{\pi}(b^2 + c^2)^{1/4}}, \quad (A23)$$

and the solution is

$$n = n_0\left\{f + \sum_{i=1}^3 M_i\cos(\Omega_Q\tau_Q + \delta_i)\right\}, \quad (A24)$$

where

$$f = 1 + \frac{1}{\sqrt{R}} - \frac{2}{\sqrt{1+R}}, \tag{A25}$$

$$\Omega_Q = 2(1+R), \tag{A26}$$

$$M_i = \frac{X_i}{\sqrt{c_i}} \left\{ 1 + \left(\frac{b}{c_i}\right)^2 \right\}^{-1/4}, \tag{A27}$$

$$b = \frac{1}{\pi}[(1+R)\{\ln(4\tau_Q) + \gamma_E - 2\} + R\ln R], \tag{A28}$$

$$\delta_i = \frac{3\pi}{4} - \frac{1}{2}\arctan\frac{c_i}{b}, \tag{A29}$$

$$X_1 = -\frac{2(1+R)}{\sqrt{2R}}, \ X_2 = \sqrt{2R}, \ X_3 = \sqrt{\frac{2}{R}}, \tag{A30}$$

$$c_1 = 1 + R, \ c_2 = 3 + R, \ c_3 = 1 + 3R. \tag{A31}$$

We can rewrite the solution in Eq. (A24) to

$$n = n_0\{f + M\cos(\Omega_Q\tau_Q + \delta)\}, \tag{A32}$$

where the amplitude and phase are

$$M = \sqrt{\left(\sum_{i=1}^3 M_i\sin\delta_i\right)^2 + \left(\sum_{i=1}^3 M_i\cos\delta_i\right)^2}, \tag{A33}$$

$$\delta = \arctan\frac{\sum_{i=1}^3 M_i\sin\delta_i}{\sum_{i=1}^3 M_i\cos\delta_i}. \tag{A34}$$

2. Solution for $0 < g_{rt} < 1$

For the case of $0 < g_{rt} < 1$, the final excitation probability p_q^f and the density of defects n should be updated by substituting Ω_Q and b in Eqs. (A26) and (A28) with

$$\Omega_Q = 2(1+R)(1-g_{rt})^2, \tag{A35}$$

$$b = \frac{1}{\pi}[(1+R)\{\ln(4\tau_Q) + 2\ln(1-g_{rt}) + \gamma_E\} \\ - 2(1-g_{rt}) + R\ln R]. \tag{A36}$$

3. Solution for $g_{rt} = g_c = 1$

In the round-trip quench protocol with $g_{rt} = g_c = 1$, we need to tackle the TDBdG equations in Eq. (16) in another way. At the end of the first stage, $t = 0$, the solutions are

$$v_q^0 = \frac{C_1\sqrt{\pi/2}}{\Gamma(1 - i\tau_Q q^2/2)} 2^{i\tau_Q q^2/2}, \tag{A37}$$

$$u_q^0 = \frac{(-1)^{1/4}C_1\sqrt{\pi}}{\sqrt{\tau_Q}q\,\Gamma(1/2 - i\tau_Q q^2/2)} 2^{i\tau_Q q^2/2}, \tag{A38}$$

where C_1 is defined in Eq. (A3) and $2^{i\tau_Q q^2/2}$ is a trivial term. And, at the end of the second stage, the solutions are

$$v_q^f = \frac{(-1)^{1/4}u_q^0}{\sqrt{2\pi\tau_Q'}q}\left(e^{-\frac{3}{4}\pi\tau_Q'q^2} - e^{\frac{1}{4}\pi\tau_Q'q^2}\right)\Gamma\left(1 - \frac{i}{2}\tau_Q'q^2\right) \\ + \frac{v_q^0}{2\sqrt{\pi}}\left(e^{-\frac{3}{4}\pi\tau_Q'q^2} + e^{\frac{1}{4}\pi\tau_Q'q^2}\right)\Gamma\left(\frac{1}{2} - \frac{i}{2}\tau_Q'q^2\right), \tag{A39}$$

$$u_q^f = \left\{ \frac{\sqrt{\tau_Q'}q\,v_q^0}{2\sqrt{\pi}(-1)^{1/4}} \frac{\Gamma\left(\frac{1}{2} - \frac{i}{2}i\tau_Q'q^2\right)}{\Gamma\left(1 - \frac{i}{2}\tau_Q'q^2\right)} + \frac{u_q^0}{\sqrt{2\pi}} \right\} \\ \times \frac{\sqrt{2\pi}\,\Gamma\left(1 - \frac{i}{2}\tau_Q'q^2\right)}{\Gamma(1 - i\tau_Q'q^2)} e^{-\frac{\pi}{4}\tau_Q'q^2}. \tag{A40}$$

The final excitation probability is still expressed by Eq. (20) but with different variables

$$A = \tfrac{1}{2}\sqrt{1 + e^{-\pi\tau_Q q^2}}\sqrt{1 - e^{-\pi\tau_Q'q^2}},$$

$$B = \tfrac{1}{2}\sqrt{1 - e^{-\pi\tau_Q q^2}}\sqrt{1 + e^{-\pi\tau_Q'q^2}},$$

and ψ that has been shown in Eq. (42). When $R = 1$, we can get a reduced excitation probability

$$p_q^f = (1 - e^{-2\pi\tau_Q q^2})\sin^2\left[\frac{\pi}{4} + \frac{\tau_Q q^2}{2}\left\{\gamma_E + \gamma_d\left(\frac{1}{2}\right)\right\}\right]. \tag{A41}$$

APPENDIX B: CALCULATION OF THE DIAGONAL AND OFF-DIAGONAL FERMIONIC CORRELATORS

By the long-wave approximation, we can rewrite the diagonal fermionic correlator in Eq. (72) to

$$\alpha_r = \int_0^\pi \frac{dq}{\pi}\cos(qr)\{2e^{-2\pi\tau_Q q^2}(e^{-2\pi\tau_Q q^2} - 1) \\ + 2(e^{-2\pi\tau_Q q^2} - e^{-4\pi\tau_Q q^2})\cos\psi\}, \tag{B1}$$

where ψ is the total dynamical phase defined in Eq. (23). Then, by utilizing the following two integrations ($m = 1, 2$),

$$\int_0^\pi \frac{dq}{\pi}\cos(qr)e^{-2m\pi\tau_Q q^2} = \sqrt{\frac{m}{\pi\hat{\xi}^2}}e^{-mr^2/\hat{\xi}^2}, \tag{B2}$$

$$\int_0^\pi \frac{dq}{\pi}e^{-2m\pi\tau_Q q^2}\cos(qr)\cos\psi = \frac{\sqrt{8}e^{-r^2/(l_m^\alpha)^2}\sin\phi_{m,r}^\alpha}{(2m\pi^2)^{1/4}\sqrt{\hat{\xi}\,l_m^\alpha}}, \tag{B3}$$

where the three lengths $\hat{\xi}$ and $l^{\alpha_{m's}}$, and the phases $\phi_{m,r^{\alpha's}}$, are defined in Eqs. (76), (77), and (75), we can get the result in Eq. (74).

For the off-diagonal fermionic correlator β_r, we first adopt the approximation

$$e^{-\pi\tau_Q q^2}\sqrt{1 - e^{-2\pi\tau_Q q^2}} \approx Yq\sqrt{2\pi\tau_Q}e^{-y\pi\tau_Q q^2} \tag{B4}$$

to make the integral analytically tractable. The two variational parameters y and Y are to be fixed. This can be done numerically [48]. Here we provide an alternative way, which demands the two sides of Eq. (B4) share the same extremum at their peaks. The left side of Eq. (B4) exhibits a peak at position $q^* = \sqrt{\frac{\ln 2}{2\pi\tau_Q}}$ with the extreme value $\frac{1}{2}$. Meanwhile, the right side of Eq. (B4) exhibits a peak at position $\tilde{q}^* = \frac{1}{\sqrt{2\pi y\tau_Q}}$ with

the extreme value $\frac{Y}{\sqrt{ye}}$. So we get two equations

$$q^* = \tilde{q}^*, \quad \frac{1}{2} = \frac{Y}{\sqrt{ye}}. \tag{B5}$$

The solutions are $y = \frac{1}{\ln 2}$ and $Y = \frac{1}{2}\sqrt{\frac{e}{\ln 2}}$. Thus, we can arrive at

$$u_q(t_f)v_q^*(t_f) \approx \sum_{m=1}^{5}(-1)^{m-1}Y_m\, q\, e^{-h_m\pi\tau_Q q^2}\sqrt{2\pi\tau_Q}$$

$$\times\, e^{i(\lambda_m' + q^2\tau_Q\lambda_m)}, \tag{B6}$$

where h_m, Y_m, λ_m', and λ_m can be found below Eq. (78) in the main text. Next, by substituting Eq. (B6) into β_r, we can deduce the integrals like

$$X_m\sqrt{2\pi\tau_Q}\int_0^{\pi}\frac{dq}{\pi}\sin(qr)\,q\,e^{-h_m\pi\tau_Q q^2}\,e^{i(\lambda_m' + q^2\tau_Q\lambda_m)}$$

$$= \frac{\sqrt{2\tau_Q}X_m r\, e^{i\phi_m^\beta(r)}}{4\{(\pi h_m\tau_Q)^2 + (\tau_Q\lambda_m)^2\}^{3/4}}\, e^{-\frac{\pi h_m\tau_Q r^2/4}{(\pi h_m\tau_Q)^2 + (\tau_Q\lambda_m)^2}}$$

$$= \frac{y_m}{\sqrt{\hat{\xi}\, l_m^\beta}}\frac{r}{l_m^\beta}\, e^{-(r/l_m^\beta)^2}\, e^{i\phi_m^\beta(r)}, \tag{B7}$$

where the lengths $l_{m^{\beta's}}$ and the phases $\phi_m^\beta(r)$ are defined in Eqs. (80) and (79).

[1] T. W. B. Kibble, J. Phys. A: Math. Gen. **9**, 1387 (1976).

[2] T. W. B. Kibble, Phys. Rep. **67**, 183 (1980).

[3] W. H. Zurek, Nature (London) **317**, 505 (1985).

[4] W. H. Zurek, Acta Phys. Pol. B **24**, 1301 (1993), https://www.actaphys.uj.edu.pl/fulltext?series=Reg&vol=24&page=1301.

[5] W. Zurek, Phys. Rep. **276**, 177 (1996).

[6] I. Chuang, R. Durrer, N. Turok, and B. Yurke, Science **251**, 1336 (1991).

[7] M. J. Bowick, L. Chandar, E. A. Schiff, and A. M. Srivastava, Science **263**, 943 (1994).

[8] V. M. H. Ruutu, V. B. Eltsov, A. J. Gill, T. W. B. Kibble, M. Krusius, Y. G. Makhlin, B. Plaçais, G. E. Volovik, and W. Xu, Nature (London) **382**, 334 (1996).

[9] C. Bäuerle, Y. M. Bunkov, S. N. Fisher, H. Godfrin, and G. R. Pickett, Nature (London) **382**, 332 (1996).

[10] R. Monaco, J. Mygind, and R. J. Rivers, Phys. Rev. Lett. **89**, 080603 (2002).

[11] A. Maniv, E. Polturak, and G. Koren, Phys. Rev. Lett. **91**, 197001 (2003).

[12] L. E. Sadler, J. M. Higbie, S. R. Leslie, M. Vengalattore, and D. M. Stamper-Kurn, Nature (London) **443**, 312 (2006).

[13] C. N. Weiler, T. W. Neely, D. R. Scherer, A. S. Bradley, M. J. Davis, and B. P. Anderson, Nature (London) **455**, 948 (2008).

[14] D. Golubchik, E. Polturak, and G. Koren, Phys. Rev. Lett. **104**, 247002 (2010).

[15] G. D. Chiara, A. del Campo, G. Morigi, M. B. Plenio, and A. Retzker, New J. Phys. **12**, 115003 (2010).

[16] S. M. Griffin, M. Lilienblum, K. T. Delaney, Y. Kumagai, M. Fiebig, and N. A. Spaldin, Phys. Rev. X **2**, 041022 (2012).

[17] L. Chomaz, L. Corman, T. Bienaimé, R. Desbuquois, C. Weitenberg, S. Nascimbène, J. Beugnon, and J. Dalibard, Nat. Commun. **6**, 6162 (2015).

[18] V. Yukalov, A. Novikov, and V. Bagnato, Phys. Lett. A **379**, 1366 (2015).

[19] N. Navon, A. L. Gaunt, R. P. Smith, and Z. Hadzibabic, Science **347**, 167 (2015).

[20] B. Damski, Phys. Rev. Lett. **95**, 035701 (2005).

[21] W. H. Zurek, U. Dorner, and P. Zoller, Phys. Rev. Lett. **95**, 105701 (2005).

[22] A. Polkovnikov, Phys. Rev. B **72**, 161201(R) (2005).

[23] J. Dziarmaga, Phys. Rev. Lett. **95**, 245701 (2005).

[24] J. Dziarmaga, Adv. Phys. **59**, 1063 (2010).

[25] R. W. Cherng and L. S. Levitov, Phys. Rev. A **73**, 043614 (2006).

[26] R. Schützhold, M. Uhlmann, Y. Xu, and U. R. Fischer, Phys. Rev. Lett. **97**, 200601 (2006).

[27] F. M. Cucchietti, B. Damski, J. Dziarmaga, and W. H. Zurek, Phys. Rev. A **75**, 023603 (2007).

[28] L. Cincio, J. Dziarmaga, M. M. Rams, and W. H. Zurek, Phys. Rev. A **75**, 052321 (2007).

[29] H. Saito, Y. Kawaguchi, and M. Ueda, Phys. Rev. A **76**, 043613 (2007).

[30] V. Mukherjee, U. Divakaran, A. Dutta, and D. Sen, Phys. Rev. B **76**, 174303 (2007).

[31] V. Mukherjee, A. Dutta, and D. Sen, Phys. Rev. B **77**, 214427 (2008).

[32] K. Sengupta, D. Sen, and S. Mondal, Phys. Rev. Lett. **100**, 077204 (2008).

[33] D. Sen, K. Sengupta, and S. Mondal, Phys. Rev. Lett. **101**, 016806 (2008).

[34] A. Polkovnikov and V. Gritsev, Nat. Phys. **4**, 477 (2008).

[35] J. Dziarmaga, J. Meisner, and W. H. Zurek, Phys. Rev. Lett. **101**, 115701 (2008).

[36] U. Divakaran and A. Dutta, Phys. Rev. B **79**, 224408 (2009).

[37] B. Damski and W. H. Zurek, Phys. Rev. Lett. **104**, 160404 (2010).

[38] W. H. Zurek, J. Phys.: Condens. Matter **25**, 404209 (2013).

[39] G. Kells, D. Sen, J. K. Slingerland, and S. Vishveshwara, Phys. Rev. B **89**, 235130 (2014).

[40] A. Dutta and A. Dutta, Phys. Rev. B **96**, 125113 (2017).

[41] A. Sinha, M. M. Rams, and J. Dziarmaga, Phys. Rev. B **99**, 094203 (2019).

[42] M. M. Rams, J. Dziarmaga, and W. H. Zurek, Phys. Rev. Lett. **123**, 130603 (2019).

[43] D. Sadhukhan, A. Sinha, A. Francuz, J. Stefaniak, M. M. Rams, J. Dziarmaga, and W. H. Zurek, Phys. Rev. B **101**, 144429 (2020).

[44] B. S. Revathy and U. Divakaran, J. Stat. Mech.: Theory Exp. (2020) 023108.

[45] D. Rossini and E. Vicari, Phys. Rev. Res. **2**, 023211 (2020).

[46] K. Hódsági and M. Kormos, SciPost Phys. **9**, 055 (2020).

[47] M. Białończyk and B. Damski, Phys. Rev. B **102**, 134302 (2020).

[48] R. J. Nowak and J. Dziarmaga, Phys. Rev. B **104**, 075448 (2021).

[49] D. Chen, M. White, C. Borries, and B. DeMarco, Phys. Rev. Lett. **106**, 235304 (2011).

[50] K. Baumann, R. Mottl, F. Brennecke, and T. Esslinger, Phys. Rev. Lett. **107**, 140402 (2011).

[51] S. Ulm, J. Roßnagel, G. Jacob, C. Degünther, S. T. Dawkins, U. G. Poschinger, R. Nigmatullin, A. Retzker, M. B. Plenio, F. Schmidt-Kaler, and K. Singer, Nat. Commun. **4**, 2290 (2013).

[52] X.-Y. Xu, Y.-J. Han, K. Sun, J.-S. Xu, J.-S. Tang, C.-F. Li, and G.-C. Guo, Phys. Rev. Lett. **112**, 035701 (2014).

[53] S. Braun, M. Friesdorf, S. S. Hodgman, M. Schreiber, J. P. Ronzheimer, A. Riera, M. del Rey, I. Bloch, J. Eisert, and U. Schneider, Proc. Natl. Acad. Sci. USA **112**, 3641 (2015).

[54] M. Anquez, B. A. Robbins, H. M. Bharath, M. Boguslawski, T. M. Hoang, and M. S. Chapman, Phys. Rev. Lett. **116**, 155301 (2016).

[55] C. Meldgin, U. Ray, P. Russ, D. Chen, D. M. Ceperley, and B. DeMarco, Nat. Phys. **12**, 646 (2016).

[56] J.-M. Cui, Y.-F. Huang, Z. Wang, D.-Y. Cao, J. Wang, W.-M. Lv, L. Luo, A. del Campo, Y.-J. Han, C.-F. Li, and G.-C. Guo, Sci. Rep. **6**, 33381 (2016).

[57] L. W. Clark, L. Feng, and C. Chin, Science **354**, 606 (2016).

[58] B. Gardas, J. Dziarmaga, W. H. Zurek, and M. Zwolak, Sci. Rep. **8**, 4539 (2018).

[59] A. Keesling, A. Omran, H. Levine, H. Bernien, H. Pichler, S. Choi, R. Samajdar, S. Schwartz, P. Silvi, S. Sachdev, P. Zoller, M. Endres, M. Greiner, V. Vuletić, and M. D. Lukin, Nature (London) **568**, 207 (2019).

[60] Y. Bando, Y. Susa, H. Oshiyama, N. Shibata, M. Ohzeki, F. J. Gómez-Ruiz, D. A. Lidar, S. Suzuki, A. del Campo, and H. Nishimori, Phys. Rev. Res. **2**, 033369 (2020).

[61] P. Weinberg, M. Tylutki, J. M. Rönkkö, J. Westerholm, J. A. Åström, P. Manninen, P. Törmä, and A. W. Sandvik, Phys. Rev. Lett. **124**, 090502 (2020).

[62] Z. Chen, J.-M. Cui, M.-Z. Ai, R. He, Y.-F. Huang, Y.-J. Han, C.-F. Li, and G.-C. Guo, Phys. Rev. A **102**, 042222 (2020).

[63] V. Y. Chernyak, N. A. Sinitsyn, and C. Sun, J. Phys. A: Math. Theor. **53**, 185203 (2020).

[64] S. Sarkar, D. Rana, and S. Mandal, Phys. Rev. B **102**, 134309 (2020).

[65] E. Lieb, T. Schultz, and D. Mattis, Ann. Phys. **16**, 407 (1961).

[66] S. Sachdev, *Quantum Phase Transitions*, 2nd ed. (Cambridge University Press, Cambridge, 2011).

[67] K. Sengupta and D. Sen, Phys. Rev. A **80**, 032304 (2009).

[68] P. Majumdar and P. Bandyopadhyay, Phys. Rev. A **81**, 012311 (2010).

[69] B. Basu, P. Bandyopadhyay, and P. Majumdar, Phys. Rev. A **86**, 022303 (2012).

[70] B. Basu, P. Bandyopadhyay, and P. Majumdar, Phys. Rev. A **92**, 022343 (2015).

[71] K. Roychowdhury, R. Moessner, and A. Das, Phys. Rev. B **104**, 014406 (2021).

[72] V. Mukherjee and A. Dutta, J. Stat. Mech.: Theory Exp. (2009) P05005.

[73] A. Das, Phys. Rev. B **82**, 172402 (2010).

[74] S. S. Hegde, H. Katiyar, T. S. Mahesh, and A. Das, Phys. Rev. B **90**, 174407 (2014).

[75] A. Russomanno, A. Silva, and G. E. Santoro, Phys. Rev. Lett. **109**, 257201 (2012).

[76] A. Lazarides, A. Das, and R. Moessner, Phys. Rev. Lett. **112**, 150401 (2014).

[77] J. Rehn, A. Lazarides, F. Pollmann, and R. Moessner, Phys. Rev. B **94**, 020201(R) (2016).

[78] A. Haldar and A. Das, Ann. Phys. **529**, 1600333 (2017).

[79] A. Haldar, R. Moessner, and A. Das, Phys. Rev. B **97**, 245122 (2018).

[80] A. Haldar, D. Sen, R. Moessner, and A. Das, Phys. Rev. X **11**, 021008 (2021).

[81] A. Haldar and A. Das, J. Phys.: Condens. Matter **34**, 234001 (2022).

[82] J. Dziarmaga, M. M. Rams, and W. H. Zurek, arXiv:2201.12540.

[83] H. T. Quan and W. H. Zurek, New J. Phys. **12**, 093025 (2010).

[84] W.-X. Liu, T. Wang, X.-F. Zhang, and W.-D. Li, Phys. Rev. A **104**, 053318 (2021).

[85] A. Francuz, J. Dziarmaga, B. Gardas, and W. H. Zurek, Phys. Rev. B **93**, 075134 (2016).

[86] J. B. Kogut, Rev. Mod. Phys. **51**, 659 (1979).

[87] P. Pfeuty, Ann. Phys. **57**, 79 (1970).

[88] B. Damski, H. T. Quan, and W. H. Zurek, Phys. Rev. A **83**, 062104 (2011).

[89] A. Dutta, A. Rahmani, and A. del Campo, Phys. Rev. Lett. **117**, 080402 (2016).

[90] Z.-P. Gao, D.-W. Zhang, Y. Yu, and S.-L. Zhu, Phys. Rev. B **95**, 224303 (2017).

[91] M.-Z. Ai, J.-M. Cui, R. He, Z.-H. Qian, X.-X. Gao, Y.-F. Huang, C.-F. Li, and G.-C. Guo, Phys. Rev. A **103**, 012608 (2021).

[92] M. Singh and S. Gangadharaiah, Phys. Rev. B **104**, 064313 (2021).

[93] S. Ebadi, T. T. Wang, H. Levine, A. Keesling, G. Semeghini, A. Omran, D. Bluvstein, R. Samajdar, H. Pichler, W. W. Ho, S. Choi, S. Sachdev, M. Greiner, V. Vuletić, and M. D. Lukin, Nature (London) **595**, 227 (2021).

[94] P. Scholl, M. Schuler, H. J. Williams, A. A. Eberharter, D. Barredo, K.-N. Schymik, V. Lienhard, L.-P. Henry, T. C. Lang, T. Lahaye, A. M. Läuchli, and A. Browaeys, Nature (London) **595**, 233 (2021).

[95] G. Semeghini, H. Levine, A. Keesling, S. Ebadi, T. T. Wang, D. Bluvstein, R. Verresen, H. Pichler, M. Kalinowski, R. Samajdar, A. Omran, S. Sachdev, A. Vishwanath, M. Greiner, V. Vuletić, and M. D. Lukin, Science **374**, 1242 (2021).

[96] K. J. Satzinger, Y.-J. Liu, A. Smith, C. Knapp, M. Newman, C. Jones, Z. Chen, C. Quintana, X. Mi, A. Dunsworth, C. Gidney, I. Aleiner, F. Arute, K. Arya, J. Atalaya, R. Babbush, J. C. Bardin, R. Barends, J. Basso, A. Bengtsson *et al.*, Science **374**, 1237 (2021).

[97] R. B. S, V. Mukherjee, U. Divakaran, and A. del Campo, Phys. Rev. Res. **2**, 043247 (2020).

[98] C. Zener, Proc. R. Soc. A **32**, 696 (1932).

[99] F. W. J. Olver, D. W. Lozier, R. F. Boisvert, and R. F. Boisvert, *NIST Handbook of Mathematical Functions* (Cambridge University Press, New York, 2010).